


PAPER WITH FULL DATA ATTACHED

Open Access



Evidence for suboceanic small-scale convection from a “garnet”-bearing lherzolite xenolith from Aitutaki Island, Cook Islands

Norikatsu Akizawa^{1,2*} , Kazuhito Ozawa¹, Tetsu Kogiso³, Akira Ishikawa⁴, Akira Miyake⁵, Yohei Igami⁵, Simon R. Wallis⁶, Takayoshi Nagaya^{2,6}, Chihiro Ohshima¹, Ryo Fujita⁴, Tatsuhiko Kawamoto⁷, Akihiro Tamura⁸, Tomoaki Morishita⁸, Shoji Arai⁸ and Atsushi Yasumoto⁵

Abstract

Garnet peridotite xenoliths have been rarely reported from suboceanic mantle. Petrographic and geochemical characteristics of garnet-bearing oceanic peridotite xenoliths provide precious information on dynamics of the suboceanic lithosphere and asthenosphere interaction. We examined a lherzolite xenolith included in olivine nephelinite lava from Aitutaki Island, a member of the Cook-Austral volcanic chain. The lherzolite xenolith contains reddish fine-grained (< 5 μm in size) mineral aggregates (FMAs) with size range of 0.5–6 mm, consisting of olivine, calcic and sodic plagioclases, aluminous spinel, native iron, and nepheline. Microstructural observations and chemical data corroborate that the FMA is a decomposed pyrope-rich garnet including chromian spinel grains with an irregular highly indented morphology in the center. The FMA is surrounded by pyroxene-poor and olivine-rich aureole. The spatial and morphological relationships of FMA and chromian spinel with pyroxene-depleted margin suggest a reaction of aluminous spinel + pyroxenes → pyrope-rich garnet + olivine, which requires a compression before decomposition of the garnet to FMA. An orthopyroxene grain shows slight but clear chemical zoning characterized by increase in Al, Ca, and Cr from the grain center to the rim. The zoning patterns of Al and Ca in the orthopyroxene grain can be modeled by diffusion-controlled solid-state reactions induced by pressure and temperature changes, keeping surface concentrations in equilibrium with the other coexisting mineral phases. The results indicate that the mantle, from which the lherzolite xenolith was derived, underwent isothermal decompression followed by a weak heating on a time scale of a few tenths of million years before the xenolith extraction. From the deduced compression and decompression histories, we hypothesize that the mantle beneath Aitutaki Island was once dragged down to a garnet-stable deep mantle region and brought up later by small-scale sublithospheric convection.

Keywords Garnet lherzolite, Oceanic lithosphere, Native iron, Mineral diffusion, Liquid immiscibility, Carbonaceous fluid, Nephelinite

*Correspondence:
Norikatsu Akizawa
akizawa@g.ecc.u-tokyo.ac.jp
Full list of author information is available at the end of the article

1 Introduction

Garnet peridotite xenoliths are of significant importance to extract information of deep lithospheric and asthenospheric mantle as they are derived from the depth deeper than ~70 km (O'Hara et al. 1971; Klemme and O'Neill 2000). The garnets in the peridotites provide useful and reliable geothermobarometry indispensable for reconstructing chemical and thermal structure of the deep lithospheric mantle (Nickel and Green 1985; Smith and Barron 1991; Griffin et al. 1999a, b; Ishikawa et al. 2004). The garnet peridotite xenoliths have been frequently reported in kimberlites mostly occurring in the cratonic region (Carswell and Dawson 1970; Boyd and Nixon 1978; Richardson et al. 1985), whereas their reports from the oceanic region are rare.

Many garnet-bearing xenoliths of pyroxenite and wehr-lite have been reported from Hawaii Islands (e.g., Sen et al. 2005), but a garnet peridotite xenolith is reported only in Oahu Island by Goto and Yokoyama (1988) without unequivocal evidence. Malaita Island in Solomon Islands is one of the rare localities yielding garnet peridotite xenoliths, which have contributed to reconstruct chemical and rheological structure of the deep lithospheric mantle beneath Ontong Java Plateau (Ishikawa et al. 2004; Ishikawa et al. 2011; Tommasi and Ishikawa 2014; Demouchy et al. 2015). Harigane et al. (2011) reported a fine-grained aggregate of spinel and orthopyroxene in a peridotite xenolith from petit-spot volcano in the northwestern Pacific Ocean. They argued that the fine-grained aggregate is of garnet origin without providing detailed petrography and mineral chemistry.

These limited studies on the oceanic garnet peridotite are insufficient to illustrate the spatial and temporal variation of the oceanic lithosphere, which is imperative to understand the evolution of lithosphere and asthenosphere boundary beneath the oceans (e.g., Fischer et al. 2010; Kawakatsu and Utada 2017; Rychert et al. 2020). Thus, we need to expand the localities and samples of oceanic garnet peridotite, and to examine their detailed petrological and geochemical characteristics. To achieve this purpose, it is crucial to look for the garnets in the peridotites, but they are in general susceptible to low pressure breakdown reaction during xenolith transportation from the mantle to the surface. Hence, reaction product after the garnet is a fundamental study target when supported by careful and exhaustive investigations to verify decomposition process.

Here, we present a peridotite xenolith from Aitutaki Island, a member of the Cook-Austral volcanic chain, where many peridotite xenoliths have been studied (Fodor et al. 1982; Snortum et al. 2019). The peridotite xenoliths contain aggregates of very fine-grained minerals, which were interpreted to be a breakdown product of

aluminous orthopyroxene in the previous studies (Fodor et al. 1982; Snortum et al. 2019). We show that they are a breakdown product of garnet in fertile peridotite with several lines of evidence from microstructural, mineralogical, and geochemical data. We then characterize the fertile garnet peridotite by determining whole-rock elemental concentrations, including highly siderophile elements (HSE) and Re–Os isotope ratio. We further clarify an ascent history of the peridotite xenolith by reproducing chemical zonings of orthopyroxene and microstructures related to reactions induced by pressure–temperature changes and fluid influxes. Combining all these results, we eventually infer the mantle dynamics beneath the South Pacific Ocean lithosphere.

2 Geological background

Aitutaki Island is an 8 km × 3 km volcanic island with an atoll lagoon located at the northwest end of the Cook-Austral volcanic chain in the Southwest Pacific Ocean (Fig. 1a). The island chain is oriented in northwest-southeast extending over ca. 2000 km. The Cook-Austral volcanic chain is composed of 13 islands: Marotiri, Rapa, Raivavae, Tubuai, Rurutu, Rimatara, Mangaia, Mauke, Mitiaro, Atiu, Rarotonga, and Aitutaki Islands (Fig. 1a). This area has been interpreted to be a superswell hosting large thermochemical anomaly in terms of seismic tomography and anomalously shallow seafloor depths of a few hundreds of meters (McNutt and Judge 1990; Adam and Bonneville 2005). This superswell is presumed to have formed above a superplume from the deep mantle. The Cook-Austral volcanic chain is located above the skirt of the large low shear velocity province (LLSVP) in the deep mantle (Torsvik et al. 2006).

The volcanic rocks of the Cook-Austral Islands were dated using K–Ar and Ar–Ar geochronometries (e.g., Duncan and McDougall 1976; Turner and Jarrard 1982; Bonneville et al. 2006; Hanyu et al. 2013; Rose and Koppers 2019). Recent determination of the volcanic ages with eliminating those affected by weathering and alteration revealed two distinctive trends in distance–age plot. They are called Macdonald trend (Marotiri + Rapa + Raivavae + Tubuai + Rurutu + Rimatara + Mangaia Islands, ages ranging from 4 to 20 Ma) and Rurutu trend (Rurutu + Mauke + Atiu + Aitutaki Islands, ages ranging from 1 to 9 Ma) (Rose and Koppers 2019). At the locations extending the two trends to 0 age, there are currently active Macdonald seamount and Arago seamount that was active at ~0.23 Ma (Bonneville et al. 2002) (Fig. 1a).

Aitutaki Island is situated on the ~107 Ma oceanic lithosphere according to the global plate model by Müller et al. (2019) (Fig. 1b). The volcanic activities of Rurutu and Aitutaki Islands show two age peaks: ~13 Ma

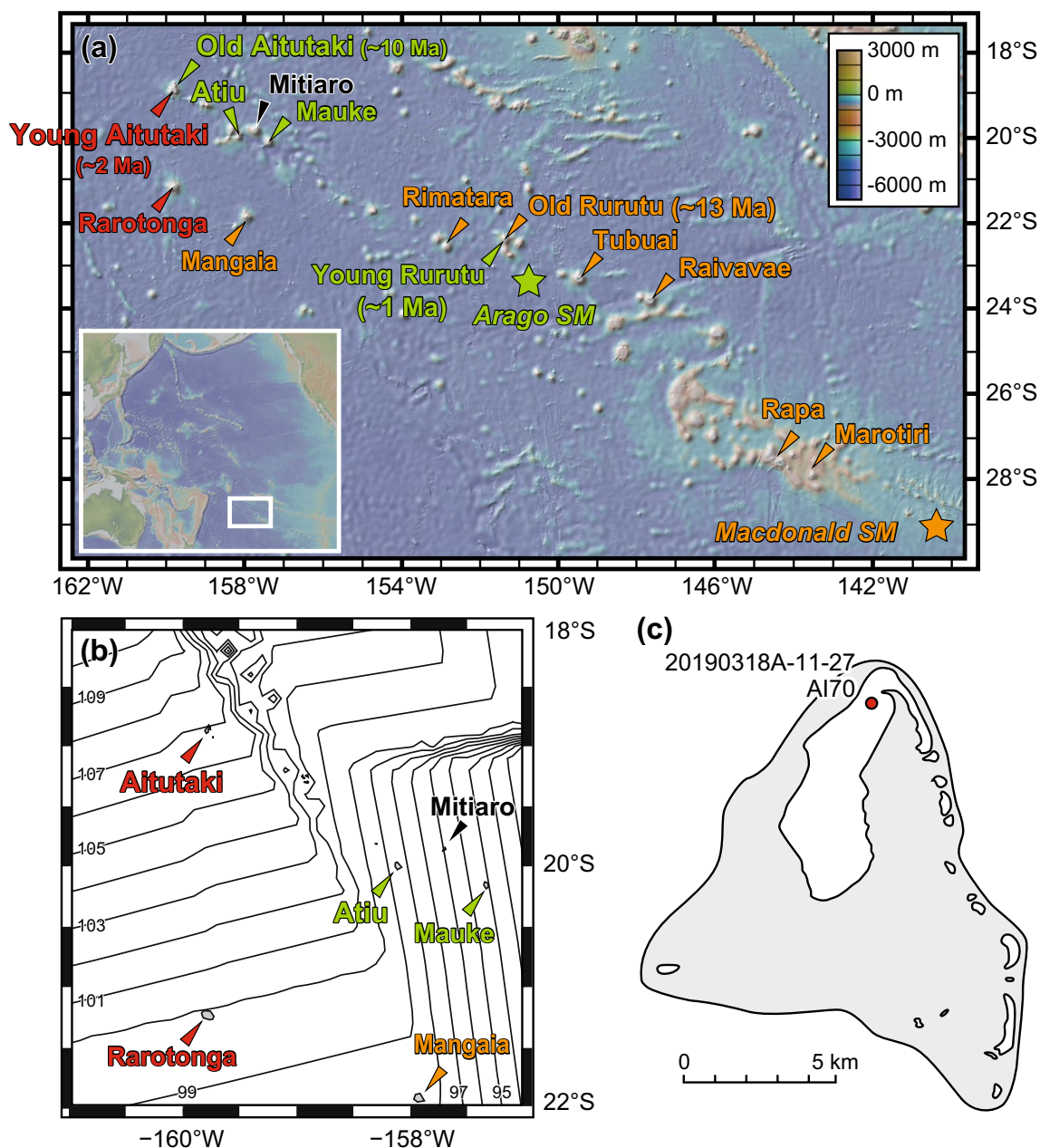


Fig. 1 Maps indicating Aitutaki Island and sample localities. **a** Magnified area of the Pacific Plate. Rectangle inset shows its wide view. The islands pointed by the orange arrows are classified as Macdonald trend, those pointed by green arrows are classified as Rurutu trend, and those pointed by the red arrows are classified as Rarotonga trend. Volcanic rocks from Mitiaro are severely weathered and no reliable age data are available (Turner and Jarrard 1982; Rose and Koppers 2019). **b** Seafloor age around Aitutaki Island. **c** Sample locations on Aitutaki Island. The images in (a) were created with GeoMapApp application (Ryan et al. 2009). The seafloor age-gridded data presented in (b) are from Müller et al. (2019). The island map in (c) is after Wood (1978). SM in (a) represents seamount

and ~1 Ma in Rurutu Island (called old Rurutu stage and young Rurutu stage, respectively), and ~9.4 Ma and ~1.4 Ma in Aitutaki Island (called old Aitutaki stage and young Aitutaki stage, respectively). In Aitutaki Island, many peridotite xenoliths are included in olivine nephelinite grouped in the young Aitutaki stage (Fodor

et al. 1982; Snortum et al. 2019). The whole-rock chemical composition of olivine nephelinite is marked by high total alkali contents ($\text{Na}_2\text{O} + \text{K}_2\text{O} > 5 \text{ wt}\%$) (Snortum et al. 2019).

The size of peridotite xenoliths from Aitutaki Island ranges from a few centimeters to 10 cm in diameter,

and they are lherzolite, harzburgite, or dunite (Fodor et al. 1982; Snortum et al. 2019). We searched xenoliths at a northern locality (18.83216° S and 159.77441° W), where olivine nephelinite lavas occur (Fig. 1c). The lavas include mantle xenoliths with megacrysts of clinopyroxene and ilmenite with ~5 cm in diameter. A lherzolite xenolith sample AI70 examined in detail in this study was included in an olivine nephelinite sample 20190318A-11-27 (Fig. 1c) with other fertile lherzolite xenoliths. The size of AI70 lherzolite is 3 cm in diameter. The olivine nephelinite consists of groundmass of clinopyroxene, nepheline, and magnetite with minor phenocrysts of olivine and clinopyroxene (Wood 1978).

3 Petrography

We examined a thin section of AI70 lherzolite having a direct contact with the host olivine nephelinite, which occupies ~10% of the entire thin section area (Fig. 2a, b). The AI70 lherzolite consists mostly of anhedral grains of olivine, orthopyroxene, clinopyroxene, and fine-grained mineral aggregate, which is called FMA hereafter (Fig. 2c). The FMA is reddish purple with the naked eye and dark red under plane-polarized transmitted light. A minor amount of spinel occurs in the AI70 lherzolite. The spinel is dark reddish brown under plane-polarized light and occurs always included in FMA grains (Fig. 2c; Supplementary Fig. S1a–d). Detailed petrography of the FMA and spinel will be described in the next section. The modal composition of AI70 lherzolite was determined from X-ray intensity maps obtained with electron probe micro analyzer (EPMA) by using GeoMAC application (<https://github.com/KazuhideMimura/GeoMAC>). It is 52.0 vol.% olivine, 22.6 vol.% orthopyroxene, 12.8 vol.% clinopyroxene, 11.7 vol.% FMA, and 0.9 vol.% spinel. Sizes of olivine, orthopyroxene, and clinopyroxene range respectively 0.1–3 mm, 0.1–4 mm, and 0.1–3 mm, which are in the ranges of the other Aitutaki lherzolite xenoliths in the olivine nephelinites. The size of FMA ranges from 0.5 to 6 mm (Fig. 2c; Supplementary Fig. S1d). The AI70 lherzolite is characterized by coarse-grained tabular equigranular texture without undulose extinction in olivine and has distinct foliation and lineation defined by shape-preferred orientation of individual grains of pyroxenes and olivine as well as aggregates of pyroxenes (Fig. 2). Individual FMA grains have rounded to subrounded outline (Fig. 2). The largest FMA grain is equidimensional (Fig. 2a–c; Supplementary Fig. S1e, f), and smaller FMA grains are elongate with long axis parallel to the foliation (Fig. 2c; Supplementary Fig. S1d). These FMA grains form a cluster, which is elongate parallel to the foliation (Fig. 2c; Supplementary Fig. S1d). The aggregate of FMA is surrounded by a domain poor in pyroxenes and rich in olivine modes (Fig. 2c; Supplementary Fig. S1d).

Orthopyroxene is locally decomposed into fine-grained (<a few tens of microns in diameter) aggregate, which is confined to an 1 cm-wide zone from the contact with the olivine nephelinite. Such orthopyroxene grains are recognized as dull brownish color under plane polarized light (Fig. 2a; Supplementary Fig. S2a, b). The decomposed aggregate consists of clinopyroxene, olivine, richterite, and glass (Supplementary Fig. S2c, d). Clinopyroxene occurring in the zone is dull greenish in color under plane polarized light and spongy associated with fine-grained (<a few tens of microns in diameter) olivine, spinel, richterite, and glass (Supplementary Fig. S2e, f). The grain boundaries in the zone of pyroxene decomposition are open as wide as 0.3 mm and filled with Na-rich (~8 wt% Na₂O) glass (Fig. 2g; grain boundary sealed with glass, hereafter). Grain boundaries sealed with minerals are developed outside the zone of pyroxene decomposition, where the grain boundaries are 0.1 to 0.2 mm-wide and consists of olivine, clinopyroxene, calcite, K-feldspar, phlogopite, spinel, and rutile with the size up to ~100 μm in diameter (Supplementary Fig. S2h–j; grain boundary sealed with minerals, hereafter).

4 Detailed petrography and chemistry of spinel-cored FMA

FMA and enclosed spinel inclusions in AI70 lherzolite show a peculiar microstructure and heterogeneity in chemical composition. They have records of changes in pressure, temperature, and chemical environment that the xenolith sample underwent in the mantle, during xenolith extraction, and transportation to the surface.

4.1 FMA (Fine-grained mineral aggregate)

FMA consists of fine-grained polyphase mineral aggregates with the size of individual grains smaller than a few microns across. Some FMA grains contain spinel grains in the center (Fig. 2), which will be described in Sect. 4.2. The FMA has diversity in chemical composition and microstructure as seen in Na, K, Ca, Mg, and Fe intensity maps (Fig. 2d–h), from which three types of FMA are recognized: K-rich, and Na and Ca-poor type (Type 1), K-poor, and Na and Ca-rich type (Type 2), and heterogeneous type with considerably higher Na than the other types (Type 3) (Fig. 2i). Each type has a respective morphology and location of occurrence as follows.

Types 1 and 2 occur in FMA grains more than 1 cm away from the contact with the host olivine nephelinite (Fig. 2i). Type 1 occurs only in the core region of the FMA grains, whereas Type 2 occupies a ~0.2 mm wide marginal region with extending toward inside to the core region, forming a dendritic network with 0.05–0.1 mm-wide branches (Figs. 2i, 3a–b). The main branches have a fracture in the middle sealed with minerals (see below

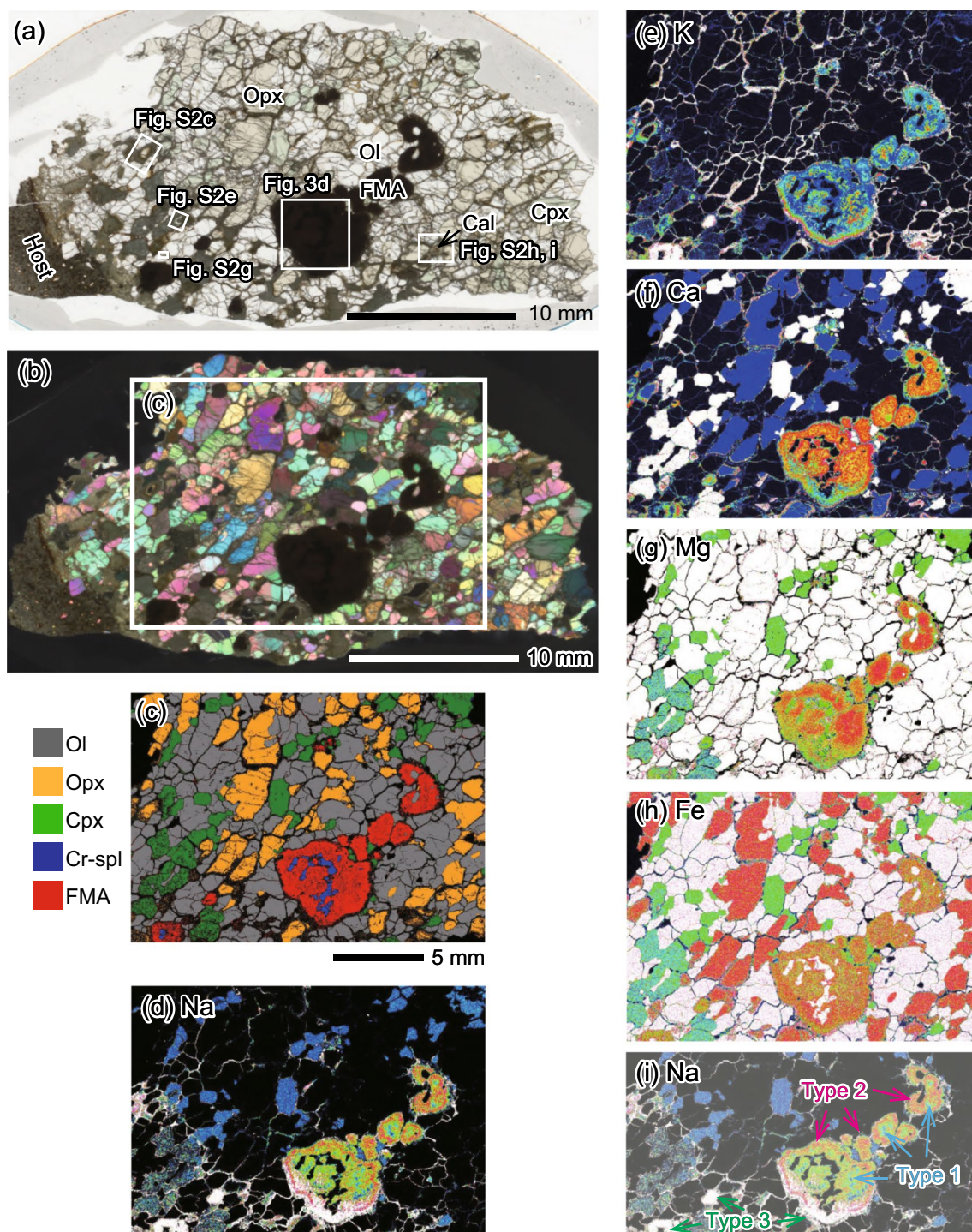


Fig. 2 Petrographic characteristics of Al₇₀ Iherzolite. **a** Thin section scan image under plane-polarized transparent light. Almost opaque areas are FMA, some of which include chromian spinel. The chromian spinel is nearly opaque in background of purple FMA. The positions of Fig. 3d and Supplementary Fig. S2c, e, g, h, and i are shown with the white squares. **b** Thin section scan image under cross-polarized transparent light. The position of **c** is shown with the white square. **c** Phase map constructed from the elemental-distribution maps of Fig. 7 using a computational method (GeoMAC, <https://github.com/KazuhideMimura/GeoMAC>). **d–h** Pseudo-color maps of Na, K, Ca, Mg, and Fe distributions, respectively. Warmer colors indicate higher elemental contents. **i** Pseudo-color map of Na with type classification of FMA based on petrography and chemical composition (see text for further details). Cal, Calcite; Cpx, Clinopyroxene; Cr-spl, Chromian spinel; FMA, Fine-grained mineral aggregate; Ol, Olivine; Opx, Orthopyroxene

for the details). The network of Type 2 decorates isolated islands of Type 1 with highly irregular morphology in the core region (Figs. 2i, 3a–b). The Na and Ca contents of Type 1 are lower, and its K content is higher than those of Type 2 (Fig. 2d–f). The abundances of these elements continuously change between the neighboring two types over the distance of 0.05–0.1 mm. The minimum Na and maximum K contents of Type 1 are attained at the center of large Type 1 islands (see the pale blue arrows in Fig. 2i), and such tendencies can be recognized irrespective of the size of Type 1 islands. Small FMA grains are completely occupied by Type 2 instead of Type 1 with the maximum K and minimum Na at the center (see the pink arrows in Fig. 2i). The Na and Ca contents of Type 2 are highest in the marginal zone of each FMA grain and tend to decrease toward the inside (Fig. 2d–f). These microstructural relationships suggest that Type 2 postdated Type 1.

Type 3 occurs mainly in FMA grains within ~1.4 cm from the contact with the olivine nephelinite, but it rarely occurs along the rim of FMA up to ~1.6 cm from the contact (Fig. 2d–f). Two smaller FMA grains placed closer to the contact with the olivine nephelinite (~1 and ~5 mm from the contact, see the green arrows in Fig. 2i) wholly belong to Type 3, whereas the largest FMA grain located more than 1 cm away from the contact has Type 3 partly along the lower left grain margin facing the contact with the olivine nephelinite (Fig. 2d–f). The Na and K contents of Type 3 decrease with distance from the contact with the olivine nephelinite when the grain margins of FMA are compared.

In each FMA grain, Na is lower, and K is higher at the core than at the margin (Fig. 2d, e). No systematic variation of Ca content in distance from the contact with the olivine nephelinite is noticed (Fig. 2f).

All the types of FMA are included in the largest FMA grain directly contacting with each other (Fig. 3a–i). Type 3 forms a dendritic network with each branch width

thinner than 50 mm and commonly as thin as 20 mm in the largest FMA (Fig. 3a–d, h). The dendritic morphology emerges from lower left grain margin, which invades ~2.5 mm into the FMA grain and extends for 5 mm along the margin with decreasing the width of invasion (Fig. 3a–d). There are differences in morphology of dendritic networks of Types 2 and 3: e.g., the branch widths are 50–100 μm and 20–50 μm , respectively (Fig. 3a–c). The dendritic networks of Types 2 and 3 are mostly complementary with each other, but Type 3 branches locally crosscut those of Type 2 (Fig. 3a–c), indicating that Type 3 postdated Type 2.

Mineral phases consisting of FMA were identified by multiple methods (Supplementary Table S1, Supplementary Figs. S3 and S4; see Supplementary methods for analytical details). All the types of FMA consist of olivine, plagioclase, and spinel with or without native iron and nepheline. Type 1 consists of polyphase aggregate of olivine (forsterite content: $100 \times \text{Mg}/(\text{Mg} + \text{Fe}^{2+})$ atomic ratio = 88), calcic plagioclase (anorthite content: $100 \times \text{Ca}/(\text{Ca} + \text{Na} + \text{K})$ atomic ratio = 87), sodic plagioclase (anorthite content = 26), and spinel (Fig. 4) with minor amounts of native iron and nepheline (Fig. 3f). Volumetric proportions of the major minerals in Type 1 are estimated to be 36.0 vol% olivine, 9.5 vol% spinel, 25.9 vol% calcic plagioclase, and 28.6 vol% sodic plagioclase (Fig. 4). The size of olivine is 0.5–2 mm, that of calcic plagioclase is 0.2–1 mm, that of sodic plagioclase is ~1 mm, and that of spinel is ~0.5 μm across in Type 1 (Figs. 3f and 4). The size of native iron and nepheline is ~5 μm across and coarser than that of the other main constituent minerals of Type 1. The olivine and calcic plagioclase are anhedral to subhedral, sodic plagioclase is anhedral, and the spinel is euhedral to subhedral (Fig. 4). The anhedral sodic plagioclase fills interstitial spaces of euhedral to subhedral grains of olivine, calcic plagioclase, and spinel, forming an interstitial network (Fig. 4). The olivine is in direct contact with both calcic and sodic plagioclases

(See figure on next page.)

Fig. 3 Detailed petrographic characteristics of Al70 lherzolite. **a–c** Pseudo-color maps of largest FMA of Na, K, and Ca distributions, respectively. The chromian spinel grains have many fractures orienting at high angles against elongate spinel morphology [see the red and yellow arrowheads facing each other in (c)]. The position of (e) is shown with the white square. **d** Backscattered electron (COMP) image of chromian spinel grains in largest FMA. It is noteworthy that native iron grains (tiny white dots) are less abundant around the chromian spinel grains and in the outer margin of FMA. The positions of (h) and (i) are shown with the white squares. **e** Magnified view of Fe and Na distribution in largest FMA. Native iron and nepheline grains are recognized by red spots and pale blue spots, respectively. Note that they tend to be in direct contact with each other. The positions of (g) and (f) are shown with the white squares. **f** High magnification COMP image of Type 1 FMA. **g** High magnification COMP image of Type 2 FMA occupying marginal region around a vein sealed with olivine, plagioclase, and native iron. **h** High magnification COMP image of Na-rich outer rim of largest FMA close to the contact with the host olivine nephelinite. The position of i is shown with the white square. **i** High magnification COMP image of Type 3 FMA. Note that constituent minerals are much coarser than those of Types 1 and 2 FMAs. **j** High magnification COMP image of chromian spinel grain shown in (d). **k** Magnified view of Ca and Al distribution in and around calcite vein in the chromian spinel grain shown in (j). Al-spl, Aluminous spinel; Cal, Calcite; Cpx, Clinopyroxene; Cr-spl, Chromian spinel; FMA, Fine-grained mineral aggregate; Native Fe, Native iron; Ne, Nepheline; Ol, Olivine; Opx, Orthopyroxene; Pl, Plagioclase

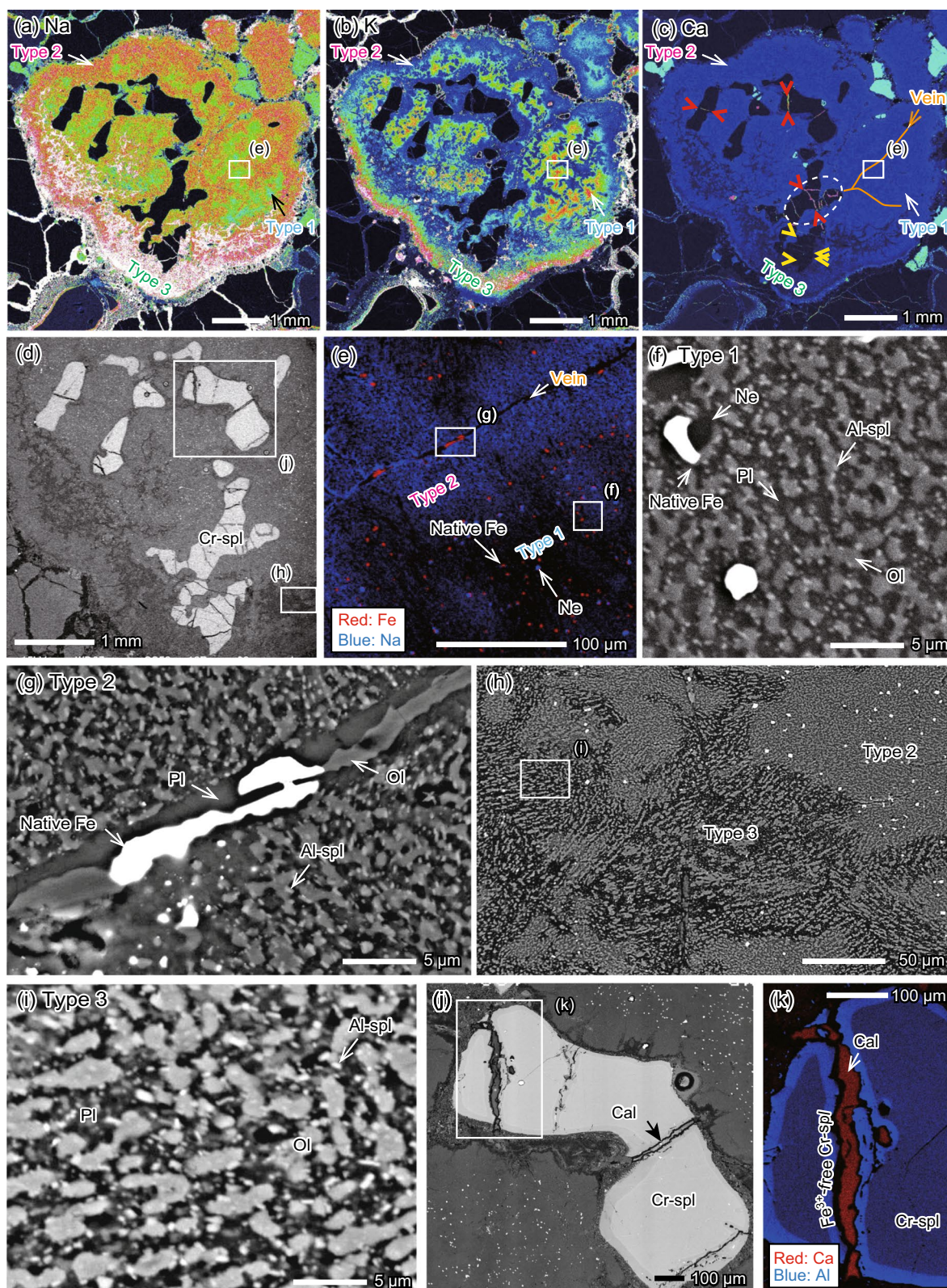


Fig. 3 (See legend on previous page.)

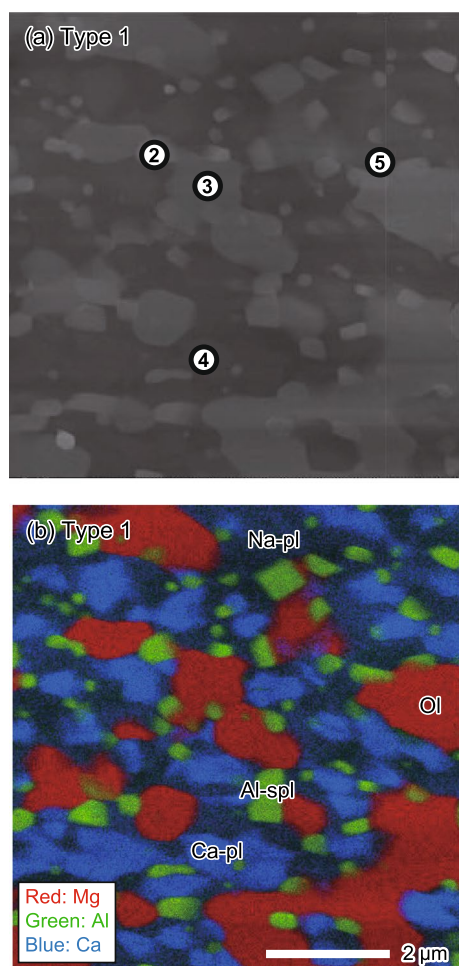


Fig. 4 Sub-micrometer-scale microstructures of Type 1 FMA in Al70 lherzolite. **a** Annular dark-field scanning transmission electron microscopy (ADF-STEM) image taken with FE-TEM. **b** Elemental distribution map of overlaying filters of red = Mg, green = Al, and blue = Ca acquired by FE-TEM-EDS. The numbers in **a** represent analytical area or spots for quantification (see Supplementary Table S1). Na-pl, Sodic plagioclase; Al-spl, Aluminous spinel; Ca-pl, Calcic plagioclase, Ol, Olivine

(Fig. 4). Large ($\sim 0.5 \mu\text{m}$ in diameter) spinel grains tend to be in contact with olivine. Shape-preferred orientation can be recognized for olivine, calcic plagioclase, and spinel (Figs. 3f, 4). Native iron and nepheline are euhedral to subhedral and are locally in direct contact with each other (Fig. 3f).

Type 2 is developed around $\sim 5 \mu\text{m}$ -thick veins that sharply cut Type 1, forming $\sim 50 \text{ mm}$ -thick Na-rich marginal zones along the veins (the orange lines in Fig. 3c; a magnified view in Fig. 3e, g). The veins are branched and construct a basic framework of network-like Type 2 (Fig. 3a–d). The veins are sealed with olivine, plagioclase,

spinel, and native iron (Fig. 3g). Type 2 is composed of the same minerals with Type 1, showing shape-preferred orientation (Fig. 3g). Native iron and nepheline are very rare or even absent near the vein and in the Na-rich marginal zone (Fig. 3e), where Type 2 is developed and Mg and Fe contents are poorer and richer than Type 1, respectively (Fig. 2g, h). The grain size of Type 2 is mostly identical to that of Type 1 (Fig. 3f, g). The minerals sealing the veins are elongate parallel to the vein direction and their size is larger (up to $\sim 10 \mu\text{m}$ in length) than the common Type 2 minerals (Fig. 3g). The olivine tends to occur in the center of the veins and is fringed by plagioclase (Fig. 3g). Native iron is present sporadically in the veins (Fig. 2g; Supplementary Fig. S5).

Type 3 located near the olivine nephelinite shows diverse mineral modes and microstructures (Fig. 3h, i). Constituent minerals are olivine, spinel, and plagioclase as in the cases of Types 1 and 2, whereas the volume fraction of sodic plagioclase is greater than those of Types 1 and 2, resulting in high Na concentration in Type 3 (Figs. 2d, 3a). No native iron and nepheline are present in Type 3 (Fig. 3h). The grain sizes of olivine, plagioclase, and spinel are $\sim 10 \mu\text{m}$ across greater than those of Types 1 and 2. The olivine shows elongate morphology, forming shape-preferred orientation radiating away from the area of Type 2 (Fig. 3h).

4.2 Spinel in FMA

Spinel shows various modes of occurrence as described above. Two of the most abundant and important spinel types are spinel incisions in FMA grains, and the other is one of the essential constituents of FMA with olivine and plagioclase. The former is more than a few hundred of microns in size (Fig. 3d) and Cr-rich ($\text{Cr}\# = \text{Cr}/(\text{Cr} + \text{Al})$ atomic ratio = ~ 0.2). The latter is smaller than \sim a few microns (Fig. 3f, g, i) and is Al-rich ($\text{Cr}\# = \sim 0.05$). We hereafter distinguish the two spinel types by calling the former chromian spinel and the latter aluminous spinel.

Two of the larger FMA grains out of 11 FMA grains have the chromian spinel in the center (Fig. 2a–c). The largest FMA grain includes several grains of chromian spinel with individual size of 0.1 to 1 mm in diameter (Fig. 3d). The chromian spinel grains are sparsely isolated in two dimensions, forming an intricate aggregate with an irregular highly indented morphology (Fig. 3d). Each grain is rounded to subrounded in shape (Fig. 3d). The same FMA grain in a cut section $\sim 1 \text{ mm}$ above the thin section plane also includes the chromian spinel grains in the center (Supplementary Fig. S1). The size of FMA grain in the cut section is ca. 6.0 mm in diameter (Supplementary Fig. S1e), which is slightly larger than the

FMA grain in the thin section (ca. 5.7 mm in diameter; Supplementary Fig. S1f), indicating that the former is closer to the grain center in three dimensions. The chromian spinel grains in the cut section are compact and massive, contrasting to grains in the thin section forming a sparsely intricate aggregate.

The crystallographic orientations of chromian spinel in the thin section were measured with a scanning electron microscope equipped with an electron-backscatter diffraction (SEM-EBSD) system (see Supplementary methods for analytical detail). The chromian spinel grains consist of distinct three clusters in terms of crystallographic orientations (Clusters A to C in Fig. 5). The misorientations between the clusters range from 30 to 60°: ~30° between Clusters A and B, 40 to 50° between Clusters A and C, and 50 to 60° between Clusters B and C, whereas those within each cluster are smaller than 20° (Fig. 5; Supplementary Fig. S6), indicating that the chromian spinel grains of Cluster A formed a single crystal with branching morphology in three dimensions. This is consistent with the three-dimensional morphology of chromian spinel as inferred above.

The chromian spinel grains in the largest FMA have sealed fractures (Fig. 3c, d). Two types of filling materials are recognized: one is calcite (see the red arrowheads facing to each other in Fig. 3c) as identified by Raman spectroscopic analysis (Supplementary Fig. S7; see Supplementary methods for analytical detail), and the other is Na-rich (~8 wt% Na₂O) glass (see the yellow arrowheads facing to each other in Fig. 3c). The fractures sealed with calcite (calcite vein, hereafter) are oriented at high angles against elongation of chromian spinel grains (Fig. 3c, d). The calcite veins do not extend into the host FMA and ends with a short (< 10 μm) protrusion into the host FMA (Fig. 3j, k).

High concentration of calcite veins (see the dotted white circle in Fig. 3c) occurs on the extension of the long extending veins in the center of Type 2 FMA (see the orange lines in Fig. 3c), suggesting that the calcite veins in the chromian spinel formed simultaneously with the veins in Type 2 FMA. In contrast, the veins sealed with Na-rich glass occur only in the chromian spinel grain placed in Type 3 FMA (see the yellow arrowheads facing to each other in Fig. 3c). The FMA bordering the chromian spinel grains belongs mostly to Type 2 FMA, having width up to 0.2 mm, where native iron and nepheline are absent or very minor in abundance (Fig. 3j), and Mg and Fe contents are lower and higher than those of Type 1 FMA, respectively (Fig. 2g, h). The chromian spinel is locally in direct contact with Type 1 FMA (Fig. 3a–c), where the native iron and nepheline are as abundant as those of normal Type 1 FMA.

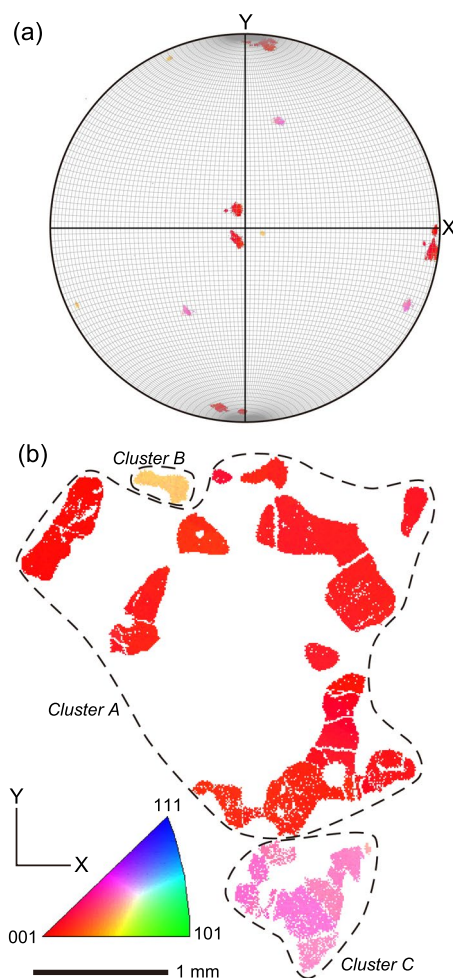


Fig. 5 Pole figure (PF) and inverse pole figure (IPF) map of chromian spinel in largest FMA of Al₇₀ Iherzolite. **a** PF of normal directions to the {001} crystal family of planes of chromian spinel indexed in **(b)**. The color contrast of measurement points corresponds to the legend color-coded according to the normal direction of the crystal plane parallel to the X-axis. The reference frame of the X-, Y- and Z-axes are the same as that in **(b)**. The axes X and Y represent long axis and short axis of the thin section, respectively. Equal-area, and lower hemisphere projections. **b** IPF map of chromian spinel. The color contrast of the measurement points corresponds to that in **(a)**. The analyzed grains can be grouped into three clusters in terms of similarity in crystallographic orientation (reddish Cluster A, pale orangish Cluster B, and pinkish Cluster C). To visually recognize the similarity in crystal orientation relationship between Clusters A to C, the data are rotated so that each of the normal axes of the (001) planes in Cluster A comes to each of the X-, Y-, and Z-axes of the pole figure. Original data before the rotation are presented in Supplementary Fig. S6

5 Whole-rock and Mineral Chemistry

5.1 Whole-rock major elements, HSE, and Re–Os isotope compositions

We conducted whole-rock chemical analyses of one olivine nephelinite (20190318A-11-27) and one Iherzolite

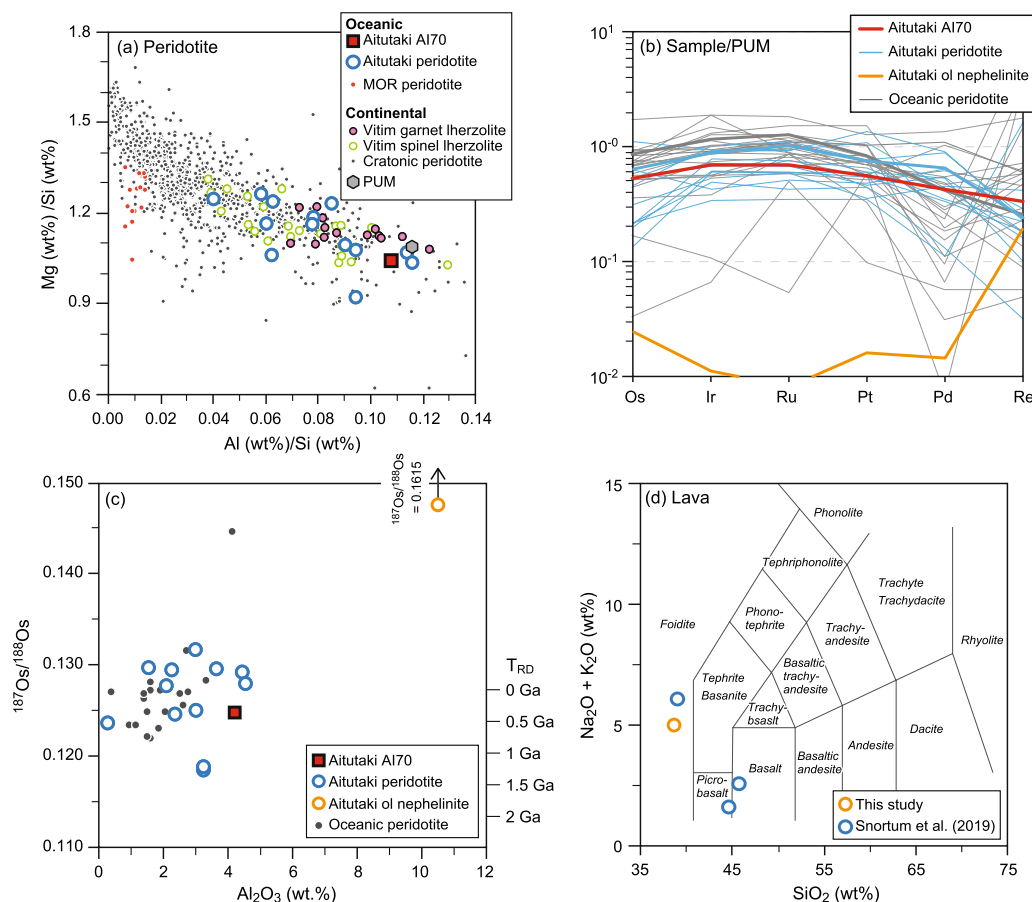


Fig. 6 Bulk chemical compositions of Aitutaki Iherzolite xenolith and its host volcanic rock from Aitutaki Island. **a** Mg/Si versus Al/Si plot (wt%). Data of peridotite from fast-spreading mid-ocean ridges (MOR) including Garrett Transform Fault (Niu and Hékinian 1997), Hess Deep Rift (Regelous et al. 2015), and Udintsev Fracture Zone (Niu 2004) are plotted. Peridotite data of cratonic region are from PetDB database (<http://www.earthchem.org/petdb>), and those of Vitim volcanic field are from Litasov and Taniguchi (2002). Primitive upper mantle (PUM) data is from McDonough and Sun (1995). **b** PUM-normalized bulk-rock highly siderophile element (HSE) patterns. Some of the patterns of Aitutaki and oceanic peridotites that are similar to the pattern of AI70 Iherzolite are highlighted by the thick pale blue and gray lines, respectively. PUM values are after Becker et al. (2006). **d** Relationship between $^{187}\text{Os}/^{188}\text{Os}$ and Al_2O_3 content. Age reference data (Re-depletion model age: T_{RD}) are shown with horizontal ticks in the right-hand side. In **(c)** and **(d)**, data of other Aitutaki samples are from Snortum et al. (2019) and those of oceanic peridotites are from Day et al. (2017). **d** Total alkali versus silica (TAS) diagram. Data shown by blue circles are volcanic rocks from Aitutaki Island reported by Snortum et al. (2019) for comparison. The thin lines represent rock classification by Le Bas et al. (1986) and Le Maitre (2002)

(AI70). The AI70 Iherzolite was powdered from a portion one centimeter away from the host olivine nephelinite. The analytical methods are summarized in Supplementary methods.

The whole-rock Al_2O_3 and CaO contents of AI70 Iherzolite are 4.19 and 3.19 wt%, respectively (Supplementary Table S2), and the Mg/Si and Al/Si weight ratios are 1.04 and 0.1, respectively, which are close to the PUM values (Fig. 6a). Reported whole-rock Mg/Si and Al/Si ratios of peridotite xenoliths from Aitutaki Island (Snortum et al. 2019) show a negative correlation and respectively range from 0.9 to 1.3 and 0.04 to 0.12 (Fig. 6a), which overlap with the ratios of peridotite xenoliths from continental

regions. The Mg/Si and Al/Si ratios of AI70 Iherzolite indicate that it is one of the most fertile Aitutaki peridotite xenoliths (Fig. 6a).

The PUM-normalized HSE pattern of AI70 Iherzolite is characterized by a smooth weakly upward convex pattern (Fig. 6b), which is comparable to some of the patterns reported from Aitutaki peridotite xenoliths (Snortum et al. 2019) and oceanic peridotites (Paquet et al. 2022) (see the thick pale blue and gray lines in Fig. 6b). The $^{187}\text{Os}/^{188}\text{Os}$ ratio of AI70 Iherzolite is 0.1248, which corresponds to 327 Ma T_{RD} (Re-depletion model age) (Fig. 6c; Supplementary Table S2). Aitutaki peridotite xenoliths including AI70 Iherzolite have diverse

$^{187}\text{Os}/^{188}\text{Os}$ ratios ranging from 0.1184 to 0.1317 (Snortum et al. 2019) mostly overlapping with the variation of oceanic peridotites (Fig. 6c).

The host olivine nephelinite is high in alkali contents (~ 5 wt% $\text{Na}_2\text{O} + \text{K}_2\text{O}$; Fig. 6d; Supplementary Table S2) and classified as foidite in the total alkali versus silica (TAS) classification diagram according to Le Bas et al. (1986). The major element composition is comparable to that of the olivine nephelinite reported by Snortum et al. (2019). The primitive upper mantle (PUM, a hypothetical undifferentiated fertile upper-mantle reservoir)-normalized HSE pattern of olivine nephelinite is characterized by a significant depletion of Os to Pd with slight depletion of Re relative to the PUM (Fig. 6b). The $^{187}\text{Os}/^{188}\text{Os}$ ratio of the olivine nephelinite is 0.1615, which is much higher than the AI70 lherzolite and other Aitutaki mantle xenoliths (Snortum et al. 2019) (Fig. 6c; Supplementary Table S2).

5.2 Mineral major-element and trace-element compositions

Spot and line analyses of major elements were conducted using an EPMA, and mineral trace-element analysis was conducted using a laser ablation-inductively coupled plasma-mass spectrometer (LA-ICP-MS). For LA-ICP-MS analyses, an analytical area size of $60\ \mu\text{m}$ was adopted for clinopyroxene and FMA, and that of $120\ \mu\text{m}$ was adopted for orthopyroxene. The analytical methods are summarized in Supplementary methods, and the results are summarized in Supplementary Tables S3–S9.

5.2.1 Thin section-scale elemental variation

AI70 lherzolite shows homogeneous distribution of elements over the thin section scale, excepting the contact area with the host olivine nephelinite, which is obviously noted by Na, Ca, and K maps (Fig. 2d–f) as well as Al, Mg, Fe, and Mg/Fe maps (Fig. 7). The Na and K heterogeneities are manifested by the variations of the grain boundaries sealed with glass or minerals. Sodium content along the grain boundaries sealed with glass is high in 1 cm-wide zone from the contact with the olivine nephelinite, and sharply drops towards the inner zone, where the grain boundaries are sealed with minerals (Fig. 2d). In contrast, K content along the grain boundaries sealed with glass show an opposite tendency, where K content along grain boundaries is low in the 1 cm-wide zone from the contact with the olivine nephelinite and abruptly increases toward the inner zone (Fig. 2e). The high K content is attributed to the presence of K-feldspar along the grain boundaries sealed with minerals (Supplementary Fig. S2h–j). Similarly, the Al, Ca, and Mg/Fe maps show that high concentration of Ca, high Mg/Fe, and low concentration of Al in the clinopyroxene

grains occurring within the 1 cm-wide zone from the contact with the olivine nephelinite (Figs. 2, 7). Such spatial elemental variations of clinopyroxenes and grain boundaries sealed with glass or minerals are strongly controlled by the distance from the contact with the olivine nephelinite. The chemical variations are characterized by abrupt changes at 1 cm from the contact with the olivine nephelinite, indicating that the inner part of AI70 lherzolite preserves pristine chemical composition and has record of processes before the AI70 lherzolite was entrapped in the olivine nephelinite magma, which modified only the marginal zone of xenolith through chemical diffusion and melt infiltration. In the following subsection, we further examine grain-scale chemical zoning patterns of pyroxene grains in the inner part of the AI70 lherzolite xenolith.

5.2.2 Zoning of major-element composition in pyroxene grains

We selected coarse orthopyroxene and clinopyroxene grains away from the contact with the olivine nephelinite for examination of grain-scale heterogeneity. The distributions of Al in the orthopyroxene and clinopyroxene grains are concentric and their Al contents increase from the core to the rim (Fig. 8a, c). The distribution of Ca in the orthopyroxene grain is also concentric and its content increases from the core to the rim (Fig. 8b), whereas the intragrain distribution of Ca in the clinopyroxene grain is unclear (Fig. 8d).

We obtained line profiles of Al and Ca for the orthopyroxene and clinopyroxene grains (Fig. 8e, f). The orthopyroxene grain is characterized by gradual increase in Al, Ca, and Cr toward the rim (0.198 to 0.203 apfu $\text{Al}_{\text{O}=\text{6}}$, 0.037 to 0.039 apfu $\text{Ca}_{\text{O}=\text{6}}$, and 0.014 to 0.015 apfu $\text{Cr}_{\text{O}=\text{6}}$) (Fig. 8e). The clinopyroxene is similarly characterized by gradual increase in Al and Cr toward the rim (0.275 to 0.282 apfu $\text{Al}_{\text{O}=\text{6}}$, and 0.027 to 0.028 apfu $\text{Cr}_{\text{O}=\text{6}}$), whereas its Ca content shows monotonous increase from a rim to the opposite rim (Fig. 8f). Average core and rim compositions in the intervals indicated by the gray bands in Fig. 8e and f are given in Supplementary Table S3.

5.2.3 Mineral major-element composition

Average forsterite and NiO contents of olivine in AI70 lherzolite are 88.9 and 0.36 wt%, which are lower than those of the other peridotites from Aitutaki Island reported by Snortum et al. (2019) (Fig. 9a; Supplementary Table S4). Olivine in the other modes of occurrences was also measured for major elements. They are (1) fine-grained olivine occurring in the decomposed orthopyroxene and clinopyroxene near the olivine nephelinite (Supplementary Fig. S2c–f), (2) fine-grained olivine

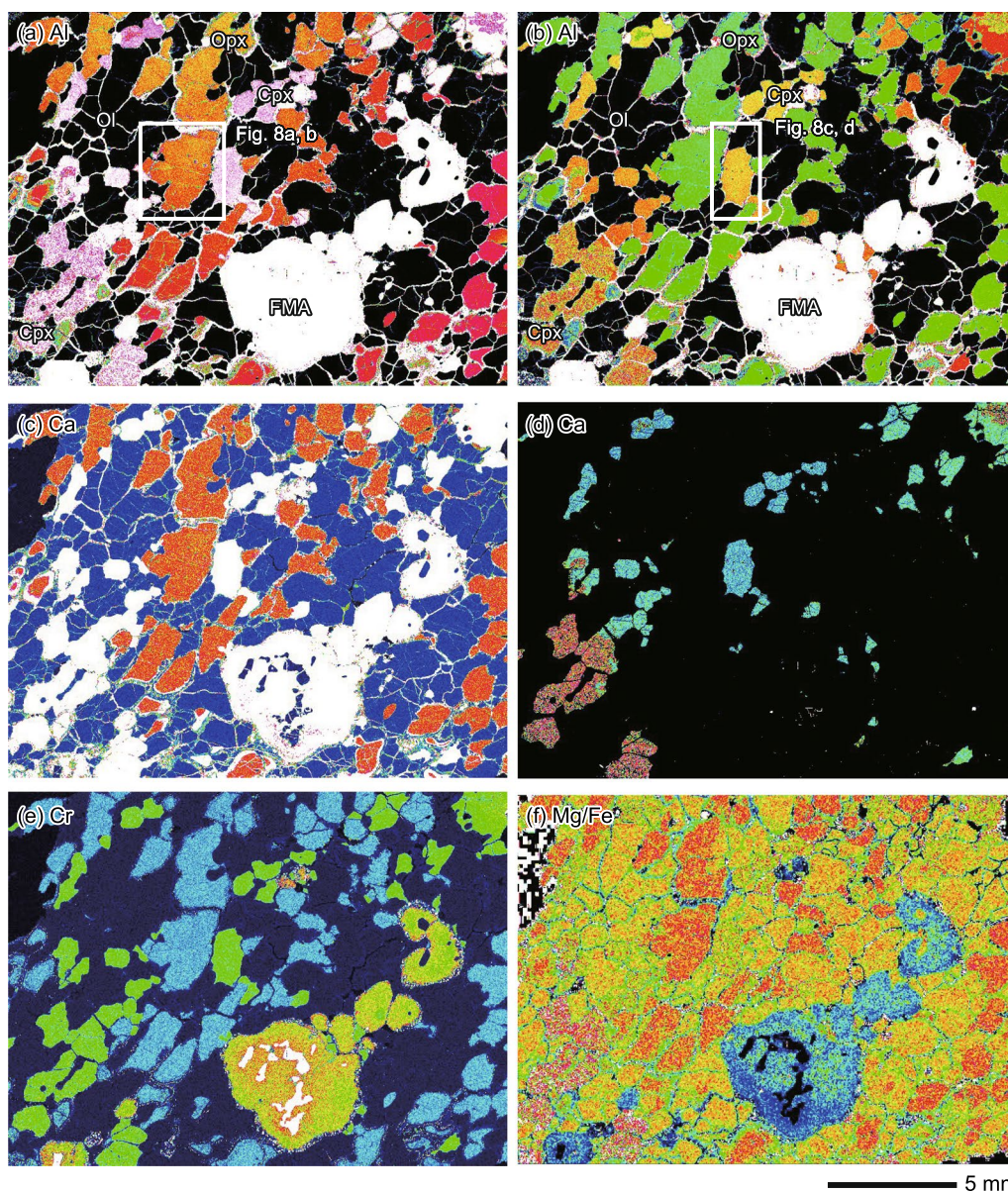


Fig. 7 Pseudo-color distribution maps of Al₇₀ lherzolite. **a** and **b** Pseudo-color maps of Al distribution with two-color coding schemes for orthopyroxene and clinopyroxene, respectively. The positions of Fig. 8a–d are shown with the white squares. **c** and **d** Pseudo-color maps of Ca distribution with two-color coding schemes for orthopyroxene and clinopyroxene, respectively. **e** and **f** Pseudo-color maps of Cr and Mg/Fe ratio distributions, respectively. Warmer colors indicate higher elemental contents. The abbreviations are the same as Fig. 3

occurring along the grain boundaries sealed with minerals (Supplementary Fig. S2h–j), and (3) olivine phenocryst in the host olivine nephelinite. All these types of olivine have lower forsterite and NiO contents than the coarse-grained olivine of the main lithology (Fig. 9a; Supplementary Table S4). The average CaO content and Mg# ($Mg/(Mg + Fe^{2+})$ atomic ratio) of orthopyroxene are 1.0 wt% and 0.89, respectively (Fig. 9b; Supplementary Table S5). Average TiO₂ and Na₂O contents of

clinopyroxene are 0.68 wt% and 1.62 wt%, respectively (Fig. 9c; Supplementary Table S6). These values are barely within the ranges of garnet lherzolites (Fig. 9b, c). The clinopyroxene of the main lithology is higher in Na₂O content than those of other modes in occurrences, which are (1) fine-grained clinopyroxene grains in the decomposed orthopyroxene (Supplementary Fig. S2c, d), (2) spongy clinopyroxene near the host olivine nephelinite (Supplementary Fig. S2e, f), (3) fine-grained

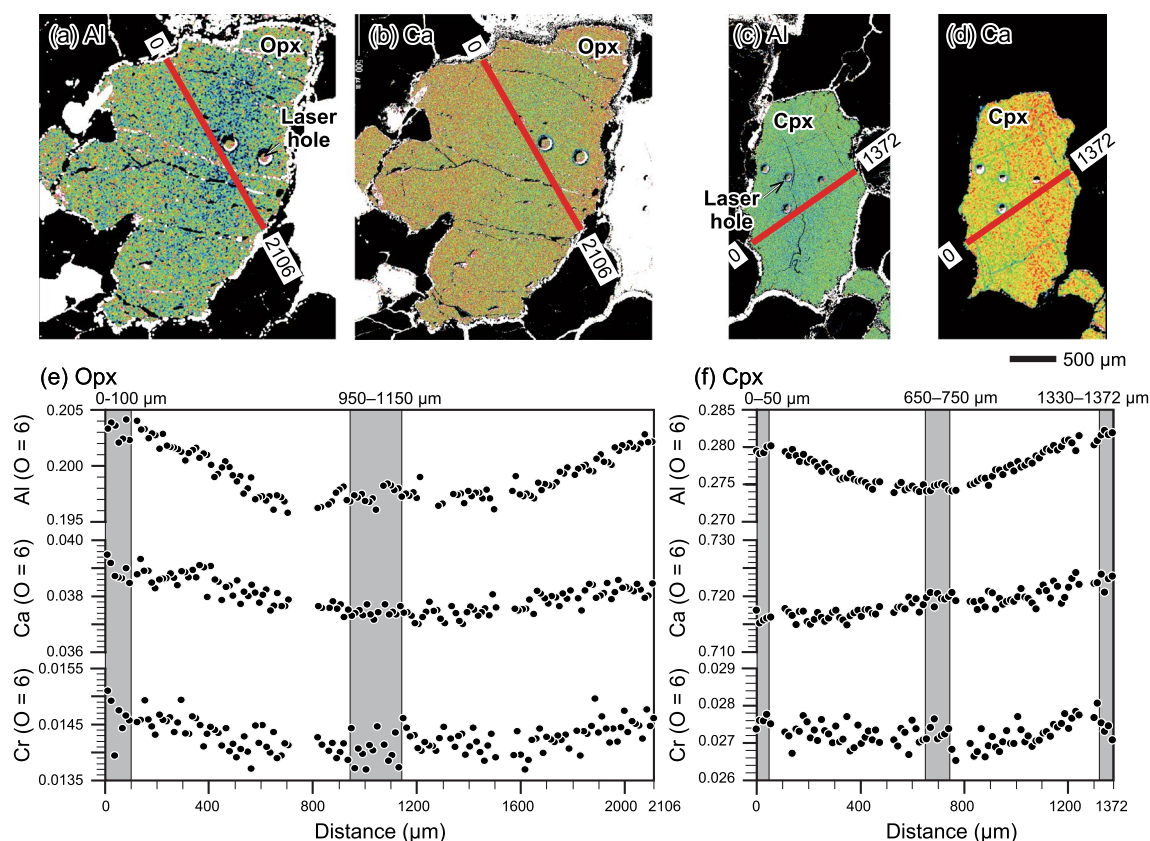


Fig. 8 Pseudo-color distribution maps and line profiles of orthopyroxene and clinopyroxene in Al₇₀ lherzolite. **a** and **b** Local pseudo-color maps of orthopyroxene for Al and Ca, respectively. **c** and **d** Local pseudo-color maps of clinopyroxene for Al and Ca, respectively. Positions are shown with the white rectangles in Fig. 7a and b. Warmer colors indicate higher elemental contents than cooler colors. **e** and **f** Line profiles of Al, Ca, and Cr in the selected orthopyroxene and clinopyroxene grains along the red lines in (a) to (d). Gray bands represent data used to calculate mean compositions for core and rim listed in Supplementary Table S3. The abbreviations are the same as Fig. 3. The cation data are calculated based on the assumption that the oxygen equals to 6

clinopyroxene along the grain boundaries sealed with minerals (Supplementary Fig. S2h–j), and (4) clinopyroxene in the groundmass of the host olivine nephelinite (Fig. 9c; Supplementary Table S6). The chromian spinel in the FMA is fringed by a few tens of micrometer-thick ferric iron-free aureole (Figs. 3k, 9d). The calcite filling the fracture developed in the chromian spinel (Fig. 3j, k) and that occurring along the grain boundaries sealed with minerals (Supplementary Fig. S2h–j) are poor in Mg (MgO < 0.5 wt%), although the former locally contains ~9 wt% MgO (Supplementary Table S8).

Bulk major-element composition of Types 1 and 2 FMAs were obtained by EPMA with defocused spot analysis and processing map analysis (Table 1; See Supplementary methods for details of analyses). The two methods give consistent results, which are similar to chemical compositions of garnets with pyrope component as high as 70% reported from garnet lherzolite

xenoliths (Table 1). Type 2 FMA contains higher Na and lower K (~2.5 wt% Na₂O, and 0.4 wt% K₂O) than Type 1 FMA (~1.7 wt% Na₂O, and 2.8 wt% K₂O) (Table 1). We modeled the bulk FMA composition from identified mineral compositions by optimizing their modal abundances (see Supplementary Table S10). The modeling results show that the bulk chemical compositions of Types 1 and 2 FMAs can be reproduced by the identified minerals with their volume fractions nearly consistent with the observed ones (Supplementary Table S10).

5.2.4 Mineral trace-element composition

Chondrite-normalized rare-earth element (REE) patterns of large orthopyroxene grains are marked by gently sloped segment from middle REE (MREE) to heavy REE (HREE) and clear depletion from MREE to light REE (LREE) irrespective of core and rim (Fig. 9e).

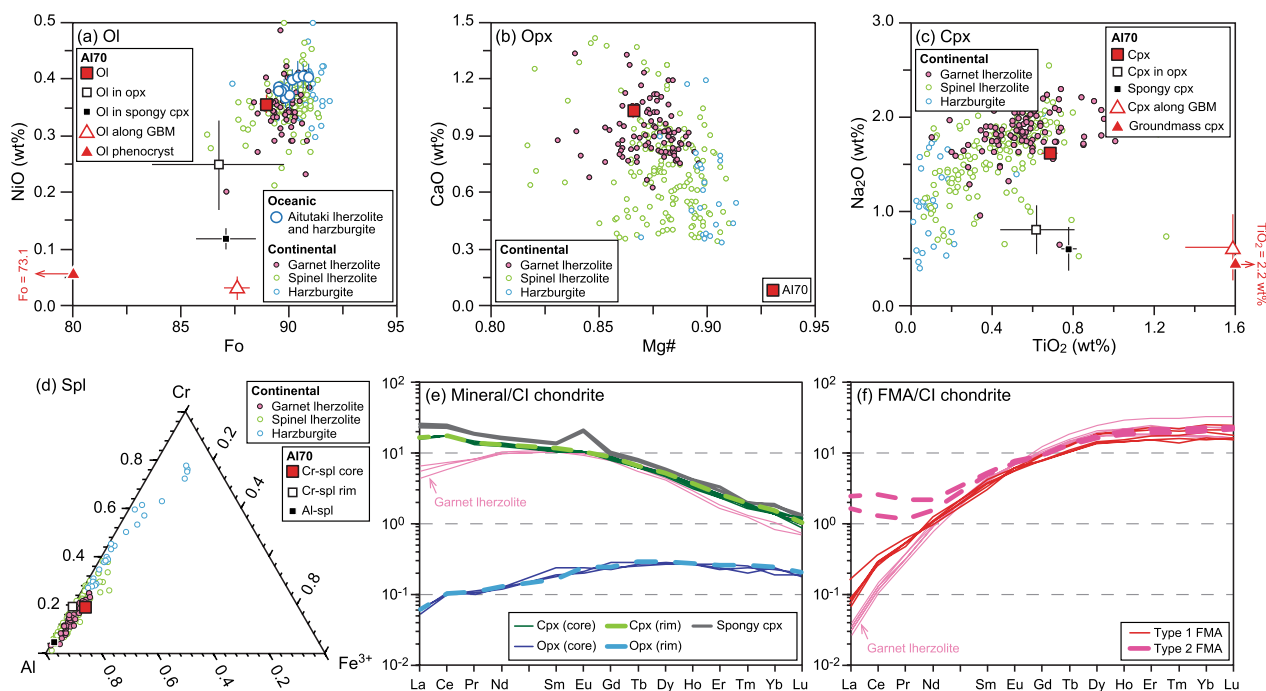


Fig. 9 Chemical compositions of minerals in Al70 Iherzolite. **a** NiO content of olivine plotted against forsterite content [$Fo = 100 \text{ Mg}/(\text{Mg} + \text{Fe}^{2+})$ atomic ratio]. **b** CaO content of orthopyroxene plotted against $Mg\#$ [$\text{Mg}/(\text{Mg} + \text{Fe}^{2+})$ atomic ratio]. **c** Na_2O content of clinopyroxene plotted against TiO_2 content. **d** Cr-Al- Fe^{3+} triangular diagram for spinel. **e** CI chondrite-normalized REE patterns of orthopyroxene and clinopyroxene. **f** CI chondrite-normalized REE patterns of FMA. Red squares in (a) to (d) are for core compositions of the main constituent minerals of the main lithology. Open squares in (a) and (c) are for fine-grained olivine and clinopyroxene grains occurring in decomposed orthopyroxene, respectively (Supplementary Fig. S2c, d). Small solid black squares in (a) and (c) are for respectively fine-grained olivine and clinopyroxene grains occurring in decomposed spongy clinopyroxene, respectively (Supplementary Fig. S2e, f). Open red triangles in (a) and (c) are for olivine and clinopyroxene grains occurring along grain boundaries sealed with minerals (GBM) coexisting with calcite (Supplementary Fig. S2h–j). Small solid red triangles in (a) and (c) represent core compositions of olivine phenocryst and groundmass clinopyroxene in the host olivine nephelinite, respectively (plotted outside of the diagrams as indicated by red arrows with values). Open square and small solid square in (d) are for rim composition of chromian spinel and fine-grained aluminous spinel in FMA, respectively. Error bars are one standard deviation, some of which are smaller than the symbols. In (a), reported olivine compositions of Aitutaki Iherzolites and harzburgites are plotted by the open blue circles (Snortum et al. 2019). Mineral data of peridotite xenoliths from Vitim volcanic field are referred from Litasov and Taniguchi (2002) for comparison. Garnet compositions and coexisting clinopyroxene compositions of Vitim garnet Iherzolites are shown in (e) and (f) for comparison with those of FMA and clinopyroxene in Al70 Iherzolite. CI chondrite values in e and f are from McDonough and Sun (1995). The abbreviations are the same as Fig. 3

Chondrite-normalized REE patterns of large clinopyroxene grains are characterized by steady enrichment from HREE to LREE irrespective of core and rim (Fig. 9e). The spongy clinopyroxene has a steeper REE pattern with higher contents than the large clinopyroxene grains and is characterized by a positive Eu anomaly (Fig. 9e). The chondrite-normalized REE patterns of bulk Type 1 FMA decline steeply from HREE to LREE, which is comparable to those of garnet in garnet Iherzolite with slightly higher values of LREEs (Fig. 9f; e.g. Litasov and Taniguchi 2002). Type 2 FMA has the same MREE to HREE contents, but is richer in LREE than Type 1 FMA, showing spoon-shaped REE patterns (Fig. 9f).

6 Garnet origin of FMA

Snortum et al. (2019) reported “nearly opaque aggregates of very fine-grained minerals” that exhibit amorphous or grainy texture at micron scale from two fertile Aitutaki Iherzolite xenoliths in olivine nephelinites (samples AK1023A and AK1023B). The aggregates enclose chromian spinel grains and have sporadic grains of Fe–Ni metals. The petrographic characteristics of the “nearly opaque aggregates of very fine-grained minerals” are essentially the same as those of FMA described in this study [cf. Figure 2a, b of Snortum et al. (2019) and Fig. 2a, b herein]. It is presumed that the “nearly opaque aggregate of very fine-grained minerals” is an FMA. The similarities of whole-rock chemical compositions and

Table 1 Bulk major-element composition of Type 1 FMA and Type 2 FMA in comparison with garnet (wt%)

Sample name	AI70				YL-2	V-860
Locality	Aitutaki, Cook Islands				Vitim volcanic field	
Note	Type 1 FMA		Type 2 FMA		Garnet	
Analytical number	4	Area 1	93	Area 2		
Analytical technique	Defocused spot	Chemical mapping technique (See Supplementary Fig. S5)	Defocused spot	Chemical mapping technique (See Supplementary Fig. S5)		
SiO ₂	42.8	42.6	42.9	42.6	40.7	42.3
TiO ₂	0.22	0.22	0.12	0.23	0.16	0.45
Al ₂ O ₃	22.7	22.9	22.9	23.0	21.7	22.9
Cr ₂ O ₃	1.41	1.22	1.18	1.26	0.94	0.57
FeO*	4.46	6.10	4.82	6.63	6.70	9.01
MnO	0.37	0.29	0.33	0.26	0.18	0.26
MgO	21.1	20.3	19.7	19.1	20.0	20.3
CaO	4.4	4.8	6.0	5.4	5.37	4.32
Na ₂ O	1.28	1.73	2.47	2.41	2.22	
K ₂ O	2.77	Not analyzed	0.36	Not analyzed		
Total	101.5	100.2	100.7	100.9	98.0	100.1
Mg#	0.894	0.842	0.879	0.856	0.842	0.801

Bulk major-element compositions of Type 1 FMA and Type 2 FMA were determined either by (1) defocused spot-analysis (20 μm in diameter) with EPMA, or (2) chemical mapping technique using QntMap developed by Yasumoto et al. (2018). Analyzed areas (Areas 1 and 2) are indicated in Supplementary Fig. S5. See Supplementary methods for analytical details. FeO* is total iron as FeO. Garnet compositions of Vitim garnet lherzolite xenoliths are referred from Litasov and Taniguchi (2002)

petrographic features, such as grain size, strong foliation or lineation, and the presence of chromian spinel only in the FMA indicate that AI70 lherzolite and AK1023A and AK1023B lherzolites are fragments derived from the same mantle material. Snortum et al. (2019) inferred that the FMA was “orthopyroxene” and interpreted that the “orthopyroxene” and enclosed chromian spinel grains were formed by a reaction between garnet and olivine by decompression from the garnet-stability field to the spinel-stability field. However, our petrographic and mineral chemical data of the FMA indicate that the FMA was not orthopyroxene. The bulk chemical composition of FMA is similar to pyrope-rich garnet in the garnet peridotites from the cratonic mantle with regard to the major elements (Table 1) and REEs (Fig. 9f, Supplementary Table S9). The strongly LREE-enriched and HREE-depleted pattern of clinopyroxene evidently suggests its coexistence with garnet (Fig. 9e). Snortum et al. (2019) described that their FMA has a bulk composition approaching to orthopyroxene, but their reported bulk composition analyzed with EDS is very different from that of orthopyroxene and rather similar to pyrope-rich garnet as it is the case for our FMA (Table 1). Therefore, we conclude that the FMA was pyrope-rich garnet before decomposition into fine-grained mineral aggregate.

The grain size of Type 1 FMA-forming minerals (< ~2 μm) (Figs. 3f, 4) is much smaller by three orders of magnitude than the chromian spinel inclusions in the FMA, which are ~1 mm across (Fig. 3d). From this fact combined with our contention mentioned above, we argue that the FMA is a breakdown product after unstable pyrope-rich garnet during or shortly before entrapment as xenolith in ascending olivine nephelinite magma and that the chromian spinel was enclosed in the garnet before its breakdown into fine-grained mineral aggregate with maintaining garnet composition (cf., Obata et al. 2013, 2014). Such isochemical breakdown of garnet is supported by our least-squares mass balance calculation (see Supplementary Table S11). The modeling results show that the bulk chemical compositions of Types 1 and 2 FMAs can be reproduced by components of garnet if Na₂O and K₂O contents are ignored or minor. It is presumed that Na and K were introduced during or after the breakdown of garnet as discussed in Sect. 8.5. Thus, we conclude that all mineral phases of the major lithology such as pyroxenes in the AI70 lherzolite had been in equilibrium with the garnet shortly before the extraction as xenolith. We present geothermobarometry of AI70 lherzolite in Sect. 7 under the assumption that the AI70 lherzolite resided in the garnet-stability field.

7 Geothermobarometry: pressure and temperature shortly before rapid xenolith exhumation

Chemical zonings of pyroxenes are caused by changes in pressure, temperature, and/or bulk chemical composition. Such changes in environment affect mineral chemical compositions of the outermost rim and are transmitted inside the grain via chemical diffusion, causing a concentric zoning pattern unless recrystallization or grain boundary migration (dissolution or growth) due to deformation and transfer reactions with a grain-boundary fluid phase occur. We investigated chemical zonings of large pyroxene grains from the center of AI70 lherzolite (Figs. 7, 8), where mineral grains are least affected by chemical modifications during events of xenolith formation and extraction such as fragmentation of mantle materials and their entrapment into a magma followed by transportation to the surface. The selected large orthopyroxene grain shows nearly concentric zoning of Al, Ca, and Cr increasing from the core to the rim (Fig. 8e). The selected large clinopyroxene grain shows similar concentric zoning of Al and Cr increasing from the core to the rim, though Ca is homogeneous in composition with minor asymmetry with maximum difference in CaO contents at both rims by ca. 0.007 apfu $\text{Ca}_{\text{O}=6}$, which is negligibly small less than 1% relative to the mean value of 0.720 apfu $\text{Ca}_{\text{O}=6}$ (Fig. 8f; Supplementary Table S3). The weak asymmetry of Ca zoning may be due to localized Ca heterogeneity along grain boundaries and does not reflect pressure and temperature changes that the entire rock underwent.

The orthopyroxene grain is zoned in Ca over the grain scale (~2 mm in diameter), which cannot be modified during xenolith extraction process if Ca diffusivity in orthopyroxene (Cherniak and Liang 2022) and short time scale of xenolith transportation (Spera 1984) are taken into consideration. Moreover, the concentric zoning of Al and Cr in both pyroxenes cannot be modified during the xenolith extraction processes, as the diffusivities of Al and Cr are much smaller than that of Ca (Cherniak and Dimanov 2010). The rim compositions of concentrically zoned pyroxene grains, therefore, record pressure and temperature (P–T) conditions shortly before the xenolith was entrapped in a magma for transportation to the surface.

The concentric zoning patterns of Ca and Al in the pyroxenes (Fig. 8) suggest decompression and/or heating before xenolith extraction since the AI70 lherzolite was in the garnet-stability field before its extraction (Gasparik 2003). The Ca, Al, and Cr profiles of the selected large orthopyroxene grain do not have a nearly flat core region in any of these elements (see Fig. 8a for Al and Fig. 8b for Ca), indicating that an application of

geothermobarometry to the core does not provide a meaningful P–T condition for long residence. The Al and Cr profiles of the selected large clinopyroxene grain also do not have a wide flat core region, which is consistent with those of the orthopyroxene if smaller grain size and slower Al and Cr diffusivity of clinopyroxene than orthopyroxene are considered (Fig. 8). Hence, the zoning patterns of pyroxenes (Fig. 8e, f) suggest that a plausible initial P–T condition is higher in pressure and/or lower in temperature than that calculated from the pyroxene cores. In order to extract P–T information from the cores of pyroxenes, initial P–T condition must be constrained by reproducing the observed zoning profiles with a diffusion model, which will be presented in Sect. 8.1.

We used two-pyroxene thermometry formulated by Brey and Köhler (1990) (T_{BKN}) because it is best calibrated for natural mantle peridotites and often used in the literatures. As discussed above in Sect. 6, the FMA was pyrope-rich garnet, and thus the pressure dependence of Al solubilities in the pyroxenes should be evaluated under the presence of garnet. We employed Al-in-orthopyroxene barometer formulated by Brey and Köhler (1990) (P_{BKN}) to estimate pressure. The chemical compositions used for our P–T estimate are mean values listed in Supplementary Table S3.

We applied the thermobarometry to the rim-rim pair of pyroxenes and obtain 1140 ± 3 °C and 2.12 ± 0.02 GPa by using the rim of low-Ca side of clinopyroxene. We calculated P–T for the core-core pair knowing that the application of geothermobarometry to the core-core pair does not provide a meaningful P–T condition for long residence as explained above and obtained 1138 ± 3 °C and 2.14 ± 0.03 GPa. The uncertainty of P–T estimates ($\pm 1\sigma$, 68% confidence interval) is evaluated with a Monte-Carlo method assuming that the source of errors is derived from analytical uncertainties with Gaussian distributions. The results are the same irrespective of which rim compositions of clinopyroxene are used. The estimated P–T conditions are within the garnet-stability field (Gasparik 1987; Zibera et al. 2013), being consistent with the assumption that the AI70 lherzolite was derived from the garnet-stability field as contended above. The Cr# of the chromian spinel is as high as 0.2 (Supplementary Table S7), which is slightly higher than that of spinel in fertile spinel lherzolite (Arai 1987) and is expected if spinel coexists with garnet in the spinel-garnet transition conditions (Nickel 1986). Although the two P–T estimates are within the errors, the Al and Ca zoning profiles without a flat core region particularly for Ca (Fig. 8a, b, e) and the contrasting P–T values calculated from the core-core and rim-rim pairs indicate that the core-core pair recorded higher pressure and lower temperature than that registered by the rim-rim pair.

8 Discussion

8.1 Pressure and temperature history before extraction of AI70 lherzolite xenolith

Gradational chemical zoning patterns of Al, Ca, and Cr recognized in the coarse orthopyroxene and clinopyroxene grains in AI70 lherzolite (Fig. 8) require decompression and/or heating in the garnet-stability field as mentioned in Sect. 7. To quantitatively estimate the P–T history of AI70 lherzolite before xenolith extraction, we used a diffusion model and tried to constrain P–T path and initial P–T condition under a constant decompression rate by reproducing the observed Al and Ca zoning patterns in the large orthopyroxene grain (Ozawa 1997, 2004; Aoki et al. 2020). Because the rim compositions reflect the P–T condition shortly before the xenolith extraction, the P–T path was constrained to reach the P–T condition estimated above for the rim-rim pair.

Successful modeling results are presented in Fig. 10. We examined various P–T paths, initial P–T conditions, and decompression rates. The decompression rate was varied from 8×10^{-8} to 6×10^{-7} GPa year⁻¹. Based on numerous simulation runs, we came to conclude that the observed zoning patterns can only be reproduced by decompression on the time scale of a few tenths of million years (0.33–0.81 million years) at decompression rates ranging from 8×10^{-8} to 2×10^{-7} GPa year⁻¹, which corresponds

to exhumation rate from 0.24 to 0.6 cm year⁻¹ (Fig. 10b). The discrepancies between the observed zoning profiles and modeled profiles might be due to a change in decompression rate during the ascent. We found that a heating in the later stage following a short isothermal decompression (Fig. 10b) is required to account for the increase in Ca content of orthopyroxene towards the rim (Fig. 10a). The initial pressure condition can be higher than 2.16 GPa as assumed from the absence of flat core regions in the zoning profiles (Fig. 8e) and modeling results shown in Fig. 10 when a slower ascent rate to reach the final depth is assumed. We conclude that the AI70 lherzolite was weakly heated during slow ascent (ca. less than 2×10^{-7} GPa year⁻¹) shortly before the rapid extraction as xenolith by a magma. The heating during decompression is consistent with the differences in P–T values calculated from the rim-rim and core-core pairs. Since the P–T dependence of Cr solubility is similar to Al in the pyroxenes (Aoki et al. 2020), the zoning patterns of Cr may be explained by the same P–T history.

8.2 Origin of chromian spinel and pyrope-rich garnet

We demonstrated above that the FMA was pyrope-rich garnet and the AI70 lherzolite resided in the garnet-stability field before it was rapidly extracted as xenolith. The chromian spinel is always enclosed in pyrope-rich

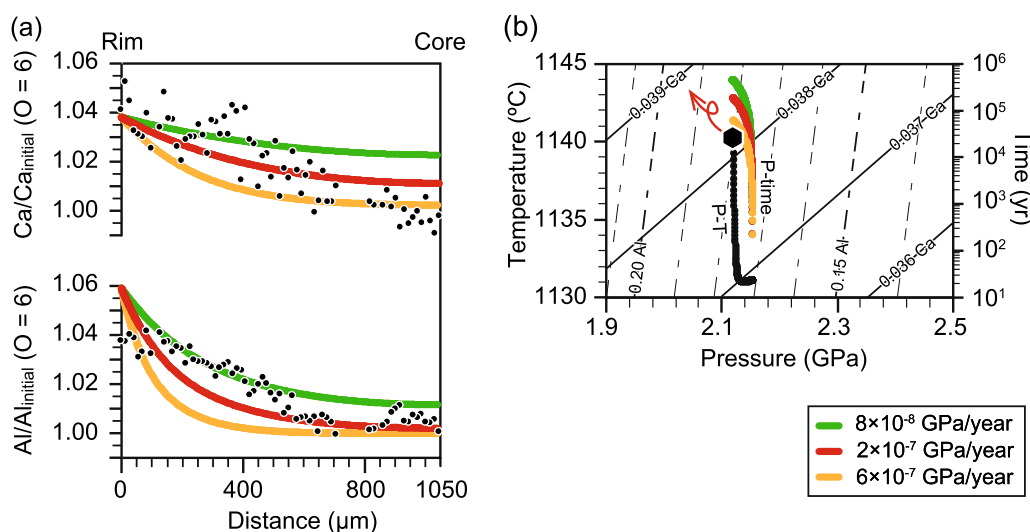
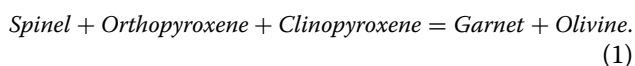


Fig. 10 Modeled Ca and Al zoning in 2.1 mm-sized orthopyroxene grain in AI70 lherzolite. Zoning profiles are shown in Fig. 8e. The analyzed Ca and Al contents are normalized by the core compositions and are plotted as black dots. The initially homogeneous orthopyroxene is assumed to have started decompression at pressure higher than the calculated pressure for the core-core pyroxene pair, whose Al₂O₃ is higher than the modeled core value. Modeling results of adiabatic upwelling with weak heating shortly before xenolith entrainment are shown in (a) and (b). The xenolith was entrapped in a magma at the depth shown by the black diamond in (b). Three different constant decompression rates of 8×10^{-8} , 2×10^{-7} , and 6×10^{-7} GPa year⁻¹ were examined in the modeling. Their pressure changes with time are shown by the colored paths denoted as “P-time”, and those with temperature are shown by the black paths denoted as “P–T” in (b). The zoning patterns of orthopyroxene are best reproduced by adiabatic mantle upwelling with weak heating at slow decompression rates (8×10^{-8} to 2×10^{-7} GPa year⁻¹ corresponding to 0.6 to 0.24 cm year⁻¹) at least in the latest stage of decompression. Isopleths of Ca and Al contents per 6 oxygens in orthopyroxene are respectively shown with the solid lines and dotted lines in the P–T space of (b) (Gasparik 2000; Aoki et al. 2020)

garnet (Fig. 2c). This garnet-spinel relationship suggests that the chromian spinel was a relict from incomplete consumption of spinel during pyrope-rich garnet formation induced by compression from the spinel-stability field to the garnet-stability field. The relict origin of the chromian spinel is supported by two petrographic observations.

First, the rounded to subrounded chromian spinel grains isolated in two dimensions in the largest FMA have a similar crystallographic orientation to form the largest cluster (Cluster A; Fig. 5), indicating that the cluster is a single crystal with very irregular and intricate three-dimensional morphology. The same FMA in a section ~1 mm above the plain of the thin section has slightly smaller, more compact, and massive morphology than those in the thin section (Supplementary Fig. S1e, f). Such morphological difference suggests that the chromian spinel has a compact and massive core decorated by an irregular highly indented fringe with crystallographic continuity in three dimensions. The morphology can be explained either by rapid growth or dissolution, but the latter possibility is more plausible because of the presence of the compact and massive core region and the occurrence completely isolated within the FMA. Second, the FMA is surrounded by olivine-rich and pyroxene-poor aureole with a few millimeters in thickness (Fig. 2a, b; Supplementary Fig. S1d). The chromian spinel grains with irregular highly indented fringe in the pyrope-rich garnet surrounded by olivine-rich zone can be attributed to the consumption of spinel and pyroxenes with the formation of garnet and olivine. The reaction is consistent with the following pressure-sensitive reaction (e.g., Kushiro and Yoder 1966):



The low-pressure stability limit of garnet peridotite for the CaO–FeO–MgO–Al₂O₃–SiO₂ (CFMAS) system and Cr-bearing natural system (MORB Pyrolite) are shown by the solid pink lines in Fig. 11a. Reaction (1) proceeds toward the right-hand side either by temperature decrease or pressure increase (Fig. 11a). If the AI70 lherzolite was derived from a domain within the lithospheric mantle, the formation of garnet can be explained by a simple cooling of the oceanic lithosphere (e.g., Neal and Nixon 1985). By contrast, a heat loss and thus temperature drop of a domain in the asthenospheric mantle is implausible at a constant depth because there is no heat sink in the asthenosphere. However, if a domain in the asthenospheric mantle adiabatically descended by convective movement, a pressure increase with trivial temperature increase may have driven the reaction (1) to the right.

As discussed in Sect. 7, the concentric zoning patterns of Ca and Al in the large pyroxene grains in the AI70 lherzolite (Fig. 8) can be reproduced by a pressure decrease in the garnet-stability field before quick xenolith extraction (Fig. 10b). The absence of flat core regions even in the Al and Cr zoning profiles in the pyroxenes substantiates that the pressure decrease continued from a deeper level than that estimated from the core-core pyroxene pair (the blue arrow pointing the black diamond 3 in Fig. 11a). It is, therefore, inferred that the mantle domain from which the AI70 lherzolite was extracted underwent a decompression from the depth deeper than ~70 km (2.16 GPa in pressure). There is no plausible mechanism to produce such uplift in the cooling oceanic lithosphere, negating the lithosphere origin of AI70 lherzolite. Therefore, we conclude that the AI70 lherzolite was derived from a domain in convecting asthenosphere adiabatically ascended just before the xenolith extraction.

Based on the above discussions, we further envisage that an asthenospheric mantle having large equant aluminous spinel grains coexisting with pyroxenes and olivine was dragged down from the spinel-stability field to the garnet-stability field deeper in the mantle. The downward movement drove the reaction (1) toward the right, resulting in the transition of aluminous spinel into pyrope-rich garnet from the margin by decomposing surrounding pyroxenes and forming olivine (see the panels 1 and 2 in Fig. 11b). Further advance of the reaction (1) probably slowed down and eventually stopped to leave chromian spinel inclusions with irregular highly indented shape as a relict in the grown garnet (see the panel 2 in Fig. 11b). The slowing and ultimate cessation of the spinel consumption was probably due to the increase in Cr# of the relict chromian spinel from ~0.1, mean value of fertile spinel peridotites (Arai 1987), to ~0.2 (Supplementary Table S7) and the inhibition of reaction progress by complete isolation of spinel from the outside of the garnet grain. The microstructure of the chromian spinel-cored garnet requires preferential formation of garnet on spinel surface (see the panel 2 in Fig. 11b). Similar microstructural relationships between spinel and garnet have been observed in a variety of different settings: garnet-fringing spinel in websterite from the Nikubuchi peridotite body in the Sanbagawa metamorphic belt, NW Japan (Yokoyama 1980); garnet-fringing spinel in a pyroxenite xenolith from the Middle Atlas, Morocco (Moukadiri and Kornprobst 1984); and corroded spinel relict in garnet in mylonitic garnet harzburgite from the Cabo Ortegal ultramafic complex, NW Spain (Ibarguchi et al. 1999).

8.3 Formation process of type 1 FMA

The FMA is composed mostly of fine-grained olivine, calcic and sodic plagioclases, and aluminous spinel

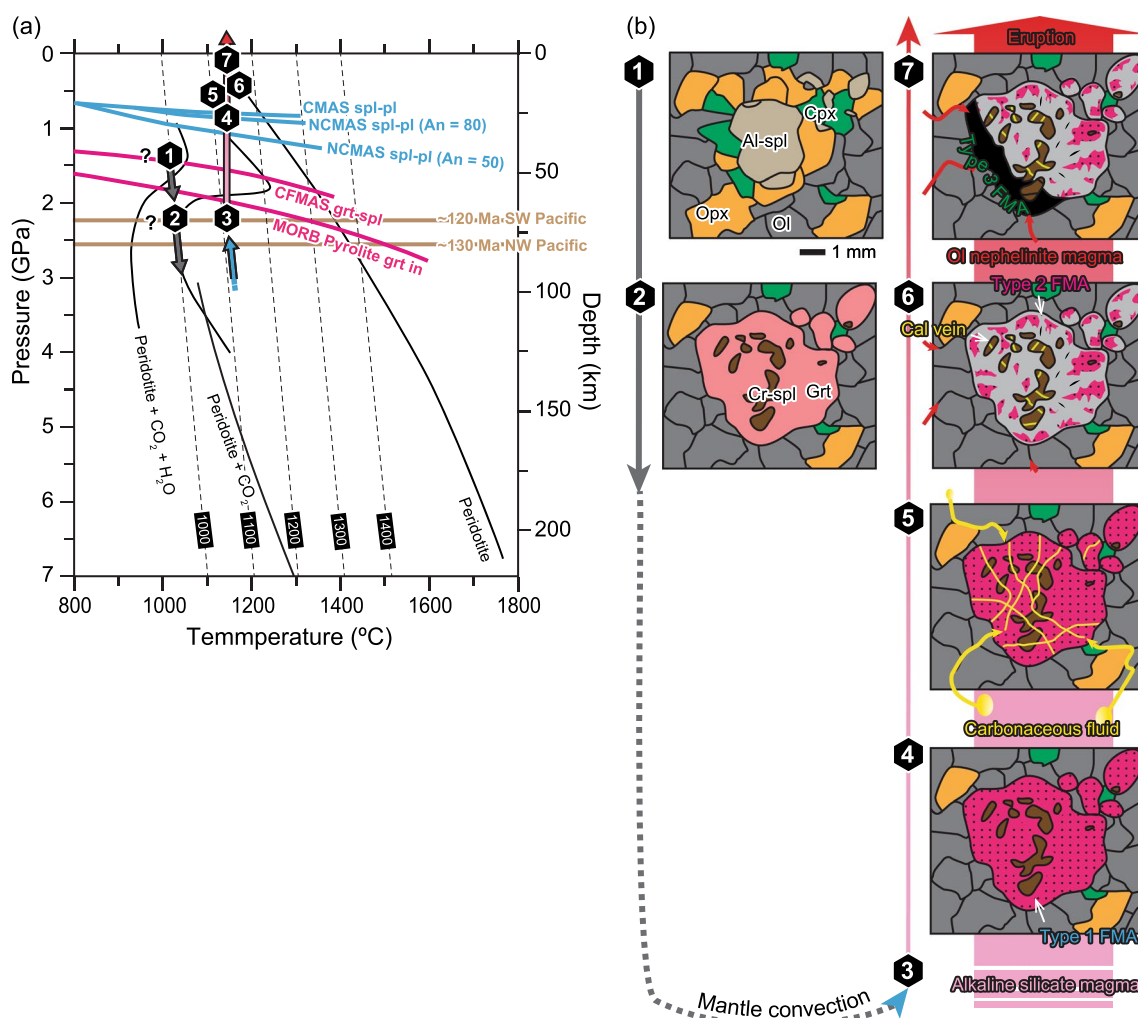
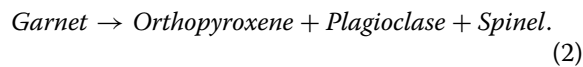


Fig. 11 Inferred thermal and decompression history of Al70 lherzolite. **a** Inferred pressure–temperature path of xenolith exhumation. Last P–T condition shortly before xenolith extraction is marked by the black diamond 3 at 1140 °C and 2.12 GPa. A path of adiabatic mantle upwelling inferred from our diffusion modeling (see Fig. 10) is portrayed with the pale blue arrow. The black diamonds 1 to 7 correspond to those in (b). See Sect. 8.7 for further details of the inferred P–T history that the Al70 lherzolite passed through in the convecting asthenospheric mantle. The mineral phase transition from garnet peridotite to spinel peridotite (grt-spl) for the Ca–Fe–Mg–Al–Si (CFMAS) system with $Mg/(Mg + Fe) = 0.9$ after Gasparik (1987) and that for MORB Pyroxite system after Zibera et al. (2013) are shown with the pink lines. The mineral phase transitions from spinel peridotite to plagioclase peridotite for the Na–Ca–Mg–Al–Si (NCMAS) system with anorthite contents ($100 \times Ca/(Ca + Na)$ atomic ratio) of plagioclase = 80, 50, and 30 after Gasparik (1987) are shown with the pale blue lines. The solidus determined by melting experiments of volatile-free peridotites and volatile-present peridotites are shown with the thin black lines (Falloon and Green 1989; Hirschmann 2000; Dasgupta and Hirschmann 2006). The thin broken black lines represent adiabatic temperature gradients for solid mantle after Herzberg and Asimow (2015). The lithosphere and asthenosphere boundaries inferred for the Southwest Pacific at ~ 120 millions of years (Herath et al. 2022) and for the Northwest Pacific at ~ 130 millions of years (Kawakatsu et al. 2009) are presented by the brown lines. **b** Inferred mineral phase transition and decompression history to form Types 1 to 3 FMAs after pyrope-rich garnet in Al70 lherzolite. See Sects. 8.3 and 8.4 for further details. Al-spl, Aluminous spinel; Cal, Calcite; Cpx, Clinopyroxene; Cr-spl, Chromian spinel; FMA, Fine-grained mineral aggregate; Grt, Garnet; Native Fe, Native iron; Opx, Orthopyroxene; Pl, Plagioclase; Spl, Spinel

(Fig. 4), which were transformed from pyrope-rich garnet. The upper pressure limit of plagioclase peridotite in the CaO – MgO – Al_2O_3 – SiO_2 (CMAS) and Na_2O –CMAS (NCMAS) systems are shown by the solid pale blue lines in pressure–temperature space (Fig. 11a). The garnet-like bulk composition of Type 1 FMA can be reproduced by

garnet components if alkalis are excluded (Supplementary Table S11), which implies isochemical breakdown of garnet and later introduction of alkalis. It is known that the garnet is isochemically decomposed into symplectic mineral aggregate by the following reaction during decompression (Obata et al. 2013):



Reaction (2) can start in the spinel-stability field above the lower pressure limit of garnet stability, forming orthopyroxene + plagioclase + spinel assemblage. The coexistence of olivine and calcic plagioclase (anorthite content up to 87.4; Supplementary Table S1) in Type 1 FMA indicates that the isochemical decomposition of garnet in the spinel-stability field was followed by transformation of orthopyroxene-bearing assemblage into the orthopyroxene-absent/olivine-bearing assemblage. The isochemical garnet breakdown to produce the FMA should have continued at pressures lower than 1.0 GPa, where plagioclase + olivine assemblage is stable (Fig. 11a). The pressure where the AI70 lherzolite resided shortly before the quick xenolith extraction estimated from the rim-rim pair of pyroxenes is 2.12 GPa. The presence of plagioclase + olivine assemblage with small grain size of constituent minerals ($\sim 5 \mu\text{m}$) in Type 1 FMA indicates that the AI70 lherzolite was quickly decompressed from ~ 2 GPa to below 1 GPa (Fig. 11a), attaining isochemical breakdown of garnet into the olivine + plagioclase + spinel assemblage observed as the FMA.

Experiments examining the decomposition of garnet showed that time scales to produce a polyphase intergrowth of orthopyroxene + spinel + anorthite in the size up to few microns are few days at temperatures of ~ 1050 °C (Ezard et al. 2022). The time scale of the isochemical decomposition of garnet documented in this study is inferred to be on the same order. Such short time scale of garnet decomposition is possible only by transportation by a magma. We hence suggest that the breakdown of garnet was driven by decompression during entrapment of the xenolith in a magma and its rapid transportation to the surface.

The olivine nephelinite hosting the AI70 lherzolite represents a magma that transported to the surface in the final stage of quick xenolith extraction. Judging from the fact that the olivine nephelinite has Fe-rich olivine phenocrysts (Fig. 9a, Supplementary Table S4), it was not equilibrated with the mantle, but was fractionated to some degrees from a parental magma. The parental magma is expected to have originated in the mantle at a pressure higher than ~ 2 GPa, where the AI70 lherzolite resided before its quick transportation. Experimentally determined liquidus temperature of olivine nephelinite magma is ~ 1400 °C at 2.25 GPa (Bultitude and Green 1971). By adopting viscosity of 2 Pa s^{-1} estimated for alkali basaltic magma at high pressure and temperature (1.4 GPa and 1440 °C, Bonechi et al. 2022) and the xenolith size of 3 cm in diameter, a velocity of magma ascent must be faster than 0.1 m s^{-1} to bring the AI70

lherzolite to the surface (e.g., Spera 1984; Russell and Jones 2023). If the olivine nephelinite magma transported the AI70 lherzolite from 70 km depth (Fig. 11a), time scale of transportation is shorter than ~ 8 days. This time scale is a maximum value as the parental magma of the olivine nephelinite that initiated the xenolith transportation could have had lower viscosity and density. Such possibility is discussed in the following subsections after clarifying the origins of Types 2 and 3 FMAs and grain boundaries sealed with glass and mineral aggregate.

8.4 Formation process of type 2 FMA and type 3 FMA

Chemical and microstructural relationships between three types of FMA show that Type 2 FMA postdated Type 1 FMA, and Type 3 FMA postdated Type 2 FMA. Since Type 2 FMA develops from the FMA margin and along the network-like fractures in the FMA grains (Fig. 3c, e), and Type 3 FMA occurs only in the FMA margin facing the contact with the olivine nephelinite (Figs. 2i, 3c), the formation of Types 2 and 3 FMAs was enhanced by infiltrations of melt or fluid. Considering that the chemical characteristics of Types 2 and 3 FMAs are distinct as shown in Sect. 4, the fluids responsible for the formation of the two types of FMA are different in chemical composition as well as in physical properties.

The localized occurrence of Type 3 FMA confined in ~ 1 cm-wide zone from the contact with the olivine nephelinite (Fig. 2i), and its latest formation than the other types of FMA implies that Type 3 FMA formed by an infiltration of the olivine nephelinite magma during the quick xenolith extraction to the surface. This is substantiated by its coexistence with open grain boundaries sealed with glass (Fig. 2d–i), which will be further discussed in Sect. 8.5.

By contrast, the fluid responsible for the formation of Type 2 FMA cannot be the olivine nephelinite magma. This is because the chemical composition of Type 2 FMA is distinct from that of Type 3 FMA and because its formation stage predated the formation of Type 3 FMA. The margin of each FMA grain is occupied by Type 2 FMA without exception (Fig. 2d–i), and the spatial variations of Na and K along the contacts between Types 1 and 2 FMAs are gradational (Fig. 3a, b). Such petrographic and chemical characteristics suggest that a fluid pervasively infiltrated into each FMA grain, replacing Type 1 FMA from the grain margin and further along fractures to form a dendritic network of Type 2 FMA (Fig. 3a–c, e, g). Because there exists the area of high concentration of calcite veins in the chromian spinel inclusions on the extension of network-like veins, from which Type 2 FMA is developed (Fig. 3c), Type 2 FMA was formed in response to the infiltration of a carbonaceous fluid with very low viscosity and surface tension. The open grain boundaries

sealed with minerals may be related to the formation of Type 2 FMA, which will be further discussed in Sect. 8.5.

8.5 Origin of grain boundaries sealed with glass or minerals and involved fluid/melt

The AI70 lherzolite has open grain boundaries, which are sealed with glass or minerals (Fig. 2d–i), suggesting that infiltration of fluid or melt along grain boundaries opened due to rapid decompression. The glass and mineral-sealed grain boundaries have intimate relationships with Types 3 and 2 FMAs, respectively, in terms of spatial distribution and chemical and mineralogical characteristics as described above. Therefore, the glass or mineral sealing the grain boundaries have unique information to reveal the nature of fluid/melt responsible for the formation of Types 2 and 3 FMAs.

The olivine nephelinite has high Na₂O content up to 4.9 wt% (Fig. 6d; Supplementary Table S2). The distribution of grain boundaries sealed with Na-rich glass (Fig. 2d; Supplementary Fig. S2g) coincides with the presence of decomposed orthopyroxene and spongy clinopyroxene (Supplementary Fig. S2c–f), and Type 3 FMA, in which native iron is absent and the constituent mineral grains are as coarse as up to ~10 μm (Fig. 3h, i). All these characteristics are confined within the 1 cm-wide zone from the contact with the olivine nephelinite (Figs. 2, 7), and hence indicate that the olivine nephelinite magma infiltrated along grain boundaries and induced decomposition of orthopyroxene and clinopyroxene with the formation of Type 3 FMA. The thickness of partially decomposed orthopyroxene and clinopyroxene is less than 1 mm (Supplementary Fig. S2c–f), which can be formed on the time scale of ~10 days (Tsuchiyama 1986). This time scale is comparable to that of xenolith transportation (a few days) as estimated in Sect. 8.3.

The grain boundaries sealed with minerals are located inside the zone of the grain boundaries sealed with Na-rich glass (Fig. 2; Supplementary Fig. S2g). The minerals filling the grain boundaries are calcite, olivine, clinopyroxene, K-feldspar, chromian spinel, rutile, and phlogopite, with their grain sizes attaining ~200 μm (Supplementary Fig. S2h–j, Supplementary Table S8). The grain boundaries are locally high in K, which is attributed to the presence of K-feldspar. None of the olivine nephelinite contains the calcite, rutile, nor phlogopite (cf., Wood 1978). The clinopyroxene occurring in the grain boundaries sealed with minerals coexists with calcite and has chemical composition distinct from those of the host olivine nephelinite in terms of CaO content (20 wt% vs. 23 wt%), Na₂O content (0.4–1.1 wt% vs. 0.5 wt%), and TiO₂ content (1.4–1.9 wt% vs. 2.2 wt%) (Fig. 9c; Supplementary Table S6). These corroborate that the olivine

nephelinite magma is irrelevant to the formation of the grain boundaries sealed with minerals, and hence we infer that the crystallization of the grain boundary-filling agent took place before the infiltration of the olivine nephelinite magma. This along with the presence of calcite in the grain boundaries sealed with minerals suggest involvement of a carbonaceous fluid before the infiltration of olivine nephelinite magma. The carbonaceous fluid had probably infiltrated into the xenolith from the outer margin of xenolith, considering that the distribution of grain boundaries sealed with minerals is controlled by the orientation of the outer margin of xenolith (Fig. 2d–i).

The chromian spinel grains in the FMA are crosscut by the calcite veins (Fig. 3d, j), and the contacting chromian spinel wall contains no ferric iron (Figs. 3k, 9d; Supplementary Table S7). These petrographic and chemical characteristics also suggest that the AI70 lherzolite was once infiltrated by the carbonaceous fluid. The calcite veins in the chromian spinel orienting at high angles against elongate spinel morphology (Fig. 3c, d, j) indicate that the carbonaceous fluid was introduced along brittle fractures developed in the chromian spinel. Since the garnet has a higher strength than the spinel (Nicolas and Poirier 1976), the relationship that the only chromian spinel inclusions have the calcite vein cannot be simply explained. The termination of calcite veins at the boundary between the chromian spinel and the host FMA corroborates that the brittle failure developed during the decomposition of garnet. Because the volume change by the garnet-breakdown reaction (2) calculated from molar volume data listed in Robie (1966) is positive, the competent chromian spinel grains embedded in the garnet might have been fractured and sucked the carbonaceous fluid, which precipitated calcite therein (see the panel 5 in Fig. 11b). The area of high concentration of calcite veins in chromian spinel inclusions is on the extension of vein (see the white dotted circle in Fig. 3c), from which Type 2 FMA was developed. This demonstrates that the formation of calcite veins in chromian spinel and Type 2 FMA are penecontemporaneous (see the panels 5 and 6 in Fig. 11b). The decomposition of calcite veins cutting the chromian spinel in the FMA within the 1 cm-wide zone from the contact with the olivine nephelinite (see the yellow arrowheads facing each other in Fig. 3c) substantiates that the formation of calcite veins and the decomposition of garnet into FMA predated the infiltration of olivine nephelinite magma into the xenolith (see the panel 7 in Fig. 11b).

We speculated above that the isochemical garnet breakdown reaction (2) occurred during rapid decompression, which might have accelerated the infiltration of carbonaceous fluid (see the panel 5 in Fig. 11b). All types

of FMA have olivine + plagioclase + spinel assemblage, but not orthopyroxene + plagioclase + spinel, which are expected from the isochemical garnet breakdown reaction (2) (Obata et al. 2013). This implies that orthopyroxene + plagioclase + spinel assemblage was replaced by olivine + plagioclase + spinel assemblage during the xenolith ascent.

The Type 2 FMA is higher in Na and LREE than Type 1 FMA (Figs. 2d, 9f; Supplementary Fig. S5). In contrast, we demonstrated that the bulk chemical composition of FMA can be explained by decomposition of pyrope-rich garnet only if alkalis are ignored (Supplementary Table S11). Therefore, it is inferred that carbonaceous fluid influx could have triggered the transformation of orthopyroxene + plagioclase + spinel into olivine + plagioclase + spinel due to the introduction of Na enhancing nucleation and growth of sodic plagioclase (Fig. 4) at lower pressures, where olivine and plagioclase are stable (see the black diamond 5 in Fig. 11a).

It is well known that the complexes comprising carbonate and alkaline silicates show bimodal distributions of the rock types (e.g., Le Bas 1987). Liquid immiscibility is a favored petrogenetic process to enhance evolved alkaline silicate magma generation in association with carbonatites (e.g., Schmidt and Weidendorfer 2018). Melting experiments showed that an alkali-rich system tends to drive the carbonate–silicate liquid immiscibility (Lee and Willie 1997; Brooker and Kjarsgaard 2011). Considering that our olivine nephelinite is high in alkali contents (~5 wt% $\text{Na}_2\text{O} + \text{K}_2\text{O}$; Fig. 6d; Supplementary Table S2), liquid immiscibility could have involved in its origin. We hypothesize that carbonaceous fluid and olivine nephelinite magma separated from an alkaline silicate magma sequentially entrapped the xenolith and transported from the garnet-stability field (Fig. 12) at a high ascent rate (0.1 m s^{-1} , see Sect. 8.3 for the calculation).

The carbonaceous fluid responsible for the formation of Type 2 FMA may have been exsolved from the ascending alkaline silicate magma expelling olivine

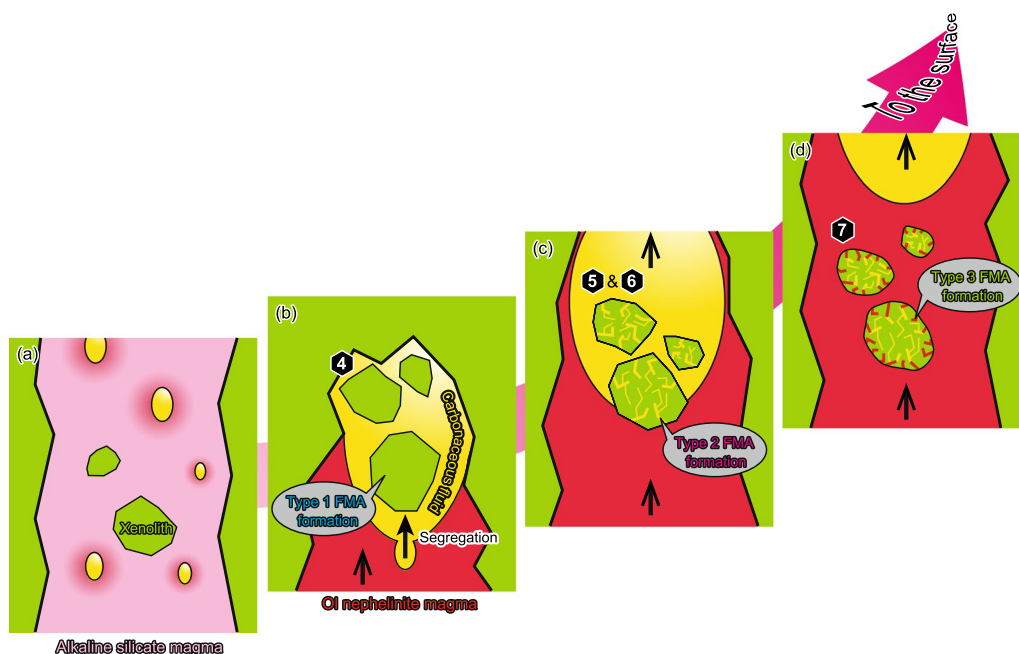


Fig. 12 A schematic illustrations of transportation processes of mantle xenoliths from Aitutaki Island. **a** Alkaline silicate magma was first formed in the asthenospheric mantle and upwelled in response to small-scale sublithospheric convection. Carbonaceous fluid and olivine nephelinite magma formed from the alkaline silicate magma via liquid immiscibility. **b** Because of low density of the carbonaceous fluid, it was segregated in the leading tip of the ascending fluid, leaving olivine nephelinite magma behind. The carbonaceous fluid broke through the mantle and ascended entrapping mantle xenoliths in the garnet-stability field. Breakdown reaction of pyrope-rich garnet to Type 1 FMA was driven by the upwelling ascent. **c** During the carbonaceous fluid transported the xenoliths in a short time, Type 2 FMA was formed by the infiltration of the carbonaceous fluid. The carbonaceous fluid was not able to hold the xenoliths for a long time because of its low viscosity and low density, facilitating the descent of the xenoliths toward the boundary with the olivine nephelinite magma. **d** The xenoliths dropped into the olivine nephelinite magma, which infiltrated into the xenoliths to form Type 3 FMA. The olivine nephelinite magma eventually brought the xenoliths to the surface. See Sect. 8.5 for further details on the transportation of Al70 lherzolite xenolith. The black diamonds 4 to 7 correspond to those in Fig. 11

nephelinite component (Fig. 12a). The carbonaceous fluid may have been quickly segregated and ascent leaving olivine nephelinite magma behind because of the low density and viscosity of carbonaceous fluid ($\sim 0.01 \text{ Pa s}^{-1}$; e.g. Kono et al. 2014) and entrapping mantle xenoliths (Fig. 12b). The carbonaceous fluid quickly infiltrated into the xenolith owing to its low viscosity (Fig. 12c), which later frozen along open grain boundaries sealed with minerals. Because of the low density and viscosity of the carbonaceous fluid, the xenoliths quickly sank through the fluid into the olivine nephelinite magma ascending behind (Fig. 12c, d). The olivine nephelinite magma transported the xenoliths to the surface, during which the olivine nephelinite magma infiltrated into the xenoliths to form Na-rich glass-sealing grain boundaries and Type 3 FMA (Fig. 12d).

8.6 Origin of native iron and nepheline in FMA

Native iron and nepheline in FMA are closely associated to each other with direct contact forming composite grains (Fig. 3f), indicating that they are genetically related and formed simultaneously as composite grain. Such native iron-nepheline composite grains in Types 1 and 2 FMAs are similar in grain size ($\sim 5 \mu\text{m}$ in diameter) and much larger than the other constituent minerals (Fig. 3f, h). The native iron-nepheline composite grains are locally absent along the FMA grain margins and around the network-like fractures forming dendritic network of Type 2 FMA. These microstructural relationships substantiate that there is no genetic link between the native iron-nepheline composite grains and Types 2 and 3 FMAs, and that they had already been present when Types 2 and 3 FMAs formed.

Metallic iron is one of the minerals that can be stable under reduced conditions below the iron-wüstite (IW) buffer. Yet, such low oxidation state is not expected in the oceanic upper mantle settings (e.g., Eguchi and Dasgupta 2018). Experimental studies performed for fertile mantle compositions as analogous to fertile AI70 lherzolite demonstrated that the metallic iron reaches saturation at high temperatures (1450–1600 °C) and pressures higher than 7 GPa (Rohrbach et al. 2007, 2011). In such cases, redox equilibrium with metallic iron is expected by disproportionation of Fe^{2+} into both Fe^0 and Fe^{3+} with preferential incorporation of Fe^{3+} into silicate phases, such as majorite garnet. This phenomenon can account for the origin of native iron-nepheline composite grains at high pressure, but there has been no report of majoritic garnet with pervasive distribution of such composite inclusions.

The homogeneous distribution of native iron-nepheline composite grains in Type 1 FMA suggests a decomposition origin from Fe and Na-rich components in the garnet

under a reducing condition (see the panel 4 in Fig. 11b). Our native iron is clearly distinct in petrography from reported native iron along cracks in garnet inclusion hosted by diamond aggregate (e.g., Jacob et al. 2004). The native iron and nepheline were later decomposed during the garnet-breakdown reaction (2) with the introduction of carbonaceous fluid along fractures, which drove the transformation of Type 1 FMA to Type 2 FMA (see the panels 5 and 6 in Fig. 11b). The native iron-nepheline composite grains are absent or depleted around the dendritic veins (Fig. 3i), around the chromian spinel inclusions (Fig. 3j), and in the outer margin of FMA (Fig. 3d), where Type 2 FMA occupies (Fig. 2g). The high Fe content and low Mg content of Type 2 FMA around the dendritic veins, chromian spinel grains, and grain margin of FMA (Figs. 2d–i) indicate that the native iron-nepheline composite grains were decomposed therein. The absence of Fe^{3+} along the chromian spinel rims and calcite veins (Fig. 3j, k) might reflect that the chromian spinel with $\sim 5 \text{ wt\% Fe}_2\text{O}_3$ (Supplementary Table S7) supplied oxygen to the native iron for oxidation reaction. Therefore, oxygen fugacity of the carbonaceous fluid is required to have been slightly higher than the IW buffer.

8.7 Implications for small-scale sublithospheric convection

In this subsection, we attempt to decipher the mantle dynamics before the exhumation of AI70 lherzolite. In Aitutaki Island, melt depletion ages (i.e., Re-depletion model age) calculated from $^{187}\text{Os}/^{188}\text{Os}$ of the peridotite xenoliths show a weak positive correlation with the whole-rock Al_2O_3 content except for two outliers (Fig. 6c). The PUM-like fertile xenoliths with high Al_2O_3 content give $T_{\text{RD}} \sim 0 \text{ Ga}$ (Fig. 6c). This implies that the fertile lherzolite including the AI70 lherzolite experienced neither melting beneath the mid-ocean ridge nor significant melting in ancient times anywhere else. The AI70 lherzolite thus does not represent an ancient, depleted mantle domain, but a fertile mantle close to PUM in terms of the bulk major-element and HSE compositions (Fig. 6a, b). It is most plausible that the AI70 lherzolite represent asthenospheric mantle that underwent negligible melting if any.

Aitutaki Island records old volcanic stage ($\sim 9.4 \text{ Ma}$) and young volcanic stage ($\sim 1.4 \text{ Ma}$) (e.g., Rose and Koppers 2019). Xenoliths are included in lavas of the young volcanic stage (Fodor et al. 1982). We advocate that a mantle upwelling could be a heat source of the young-stage volcanism. The weak heating inferred from the diffusion modeling of large orthopyroxene grain (Fig. 10) occurred just before the extraction of xenoliths. The weak heating is attributed to segregation and transportation of parental alkaline silicate magma in the upwelling mantle,

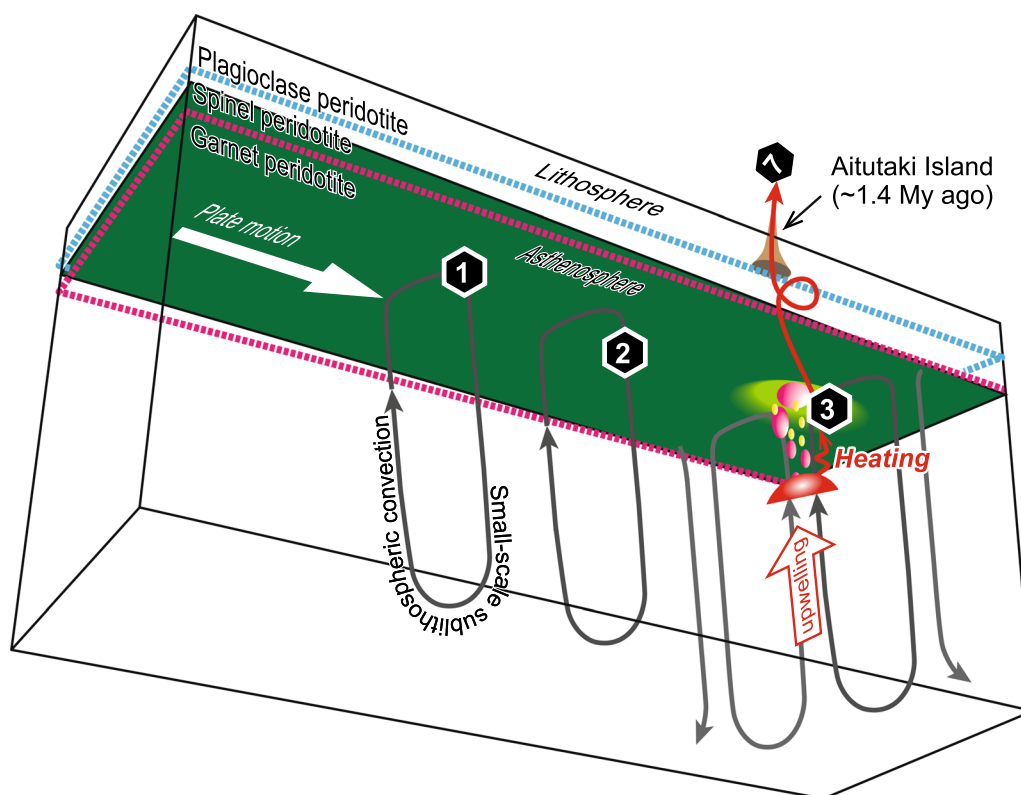


Fig. 13 A schematic mantle dynamics model inferred from AI70 lherzolite. Modified after Ballmer et al. (2007). See Sect. 8.7 for further details of the inferred small-scale sublithospheric convection roll aligned along the Cook Islands. The black diamonds 4 to 7 correspond to those in Fig. 11. Not to scale

from which the olivine nephelinite magma of the young volcanic stage was derived (Fig. 13).

Since the decompression rate of the mantle estimated from the AI70 lherzolite ($\sim 0.6 \text{ cm year}^{-1}$) is ~ 13 times slower than the velocity of the Pacific Plate ($\sim 8 \text{ cm year}^{-1}$, Zahirovic et al. 2015), we envisage that the AI70 lherzolite was sampled from part of slowly convecting mantle just beneath the lithosphere and asthenosphere boundary when the upwelling mantle impinged the base of lithosphere. The depth of lithosphere and asthenosphere boundary estimated for the Southwest Pacific by seismic observation (Herath et al. 2022) is similar to the depth at which the AI70 lherzolite resided shortly before the quick extraction (see the solid brown horizontal line in pressure–temperature space in Fig. 11a). The adiabatically upwelled asthenospheric mantle induced formation of an alkaline silicate magma parental to the host olivine nephelinite (Fig. 11b).

Garnet including dendritic chromian spinel inclusions before the decomposition of garnet into FMA is most plausibly explained by growth of garnet by consumption of spinel and pyroxenes, which is represented by the reaction (1) proceeding to the right by pressure increase (see

the panels 1 and 2 in Fig. 11b). We here speculate that the asthenospheric mantle is circulating beneath the oceanic lithosphere. There are two circulation patterns of mantle flow in the oceanic region: (1) spherical vortex caused by mantle plume (e.g., Campbell and Griffith 1990; Agrusta et al. 2013), or (2) small-scale sublithospheric convection (SSC) (e.g., Richter and Parsons 1975). As a hotter mantle plume consists of a large bulbous head and narrow feeder conduit, a colder thin boundary layer of adjacent mantle is heated by conduction until its temperature and density get comparable to the plume source, and then it is forced to stirred by a recirculating flow within the plume head (Campbell et al. 1989). Along the Cook-Austral volcanic chain, two age-progressive Macdonald trend and Rurutu trend with EM (enriched mantle) to HIMU (high μ or high $^{238}\text{U}/^{204}\text{Pb}$) affinities are identified (Fig. 1a) (Jackson et al. 2020). Thus, the plume-induced radial flow could have contributed to the convective motion inferred from the AI70 lherzolite. However, if this is the case, the AI70 lherzolite was intensely heated and melted, as the potential temperature of the plume is estimated to be hotter than the adjacent mantle in the range of 1500–1700 °C [cf., White (2010) and references therein]. However, none

of intense heating nor concomitant severe melt depletion are recognized in the AI70 lherzolite.

In the Earth's upper mantle, SSC can develop as instabilities of the thickened thermal boundary layer grown beneath old oceanic lithosphere. The convective rolls are aligned by plate motion (Richter and Parsons 1975). In contrast to the plume-induced radial flow model discussed above, the SSC model does not require any abnormal heating event. Short-lived (~20 Ma) volcanism in the Cook-Austral volcanic chain is also explained by SSC model (Ballmer et al. 2007). In conclusion, we argue that the fertile asthenospheric mantle in the oceanic region is convecting in response to SSC (Fig. 13) and generated an alkaline silicate magma parental to the olivine nephelinite (see Sect. 8.5). Onset of SSC is classically deduced from the timing of flattening (~70 Ma) on the oceanic depth and heat flow profiles against the seafloor age (e.g., Stein and Stein 1992). In this regard, SSC can occur beneath Aitutaki Island located in mature oceanic lithosphere (~107 Ma, Fig. 1b).

9 Conclusions

We examined a lherzolite xenolith included in olivine nephelinite lava from Aitutaki Island, Cook Islands. The lherzolite xenolith contains reddish fine-grained mineral aggregates (FMAs), which were classified into three types based on petrography, microstructure, and chemical characteristics. The FMA grains are surrounded by olivine-rich and pyroxene-poor zone and has clusters of anhedral chromian spinel grains as inclusions. No chromian spinel occurs outside the FMA grains. The chromian spinel grains are isolated from each other in two dimensions, but have clusters with similar crystallographic orientations, suggesting they originally formed large equant single grains, which were later partly decomposed to those in irregular three-dimensional morphology. Bulk major-element and trace-element compositions of FMA are close to those of pyrope-rich garnet in the garnet-bearing peridotite. These petrographic and geochemical observations corroborate that the FMA is decomposed pyrope-rich garnet, which was transformed from an aggregate of aluminous spinel and pyroxenes leaving the olivine margin and chromian spinel inclusions.

Large orthopyroxene and clinopyroxene grains show slight but clear chemical heterogeneity: increases in Al, Ca, and Cr from the grain center to the rim in the orthopyroxene grain, and increases in Al and Cr from the grain center to the rim with a monotonous increase in Ca in the clinopyroxene grain. The Al and Ca zoning patterns of orthopyroxene were reproduced by a diffusion model with keeping surface concentration in equilibrium with the other coexisting mineral phases under

decompression with weak heating. The decompression is estimated to have occurred on a time scale of a few tenths of million years. Because the reaction of pyroxenes + aluminous spinel \rightarrow olivine + pyrope-rich garnet resulted from an increase in pressure, we hypothesize that the asthenospheric mantle was initially descended and then ascended by small-scale sublithospheric convection controlled by the oceanic plate motion. The last pressure–temperature condition shortly before xenolith exhumation was estimated to have been 1140 °C and 2.12 GPa. This condition is within the garnet-stability field, being consistent with the FMA origin as garnet. It is also consistent with the depth of lithosphere and asthenosphere boundary on the Pacific Plate determined from seismic observations. The FMA was formed later during quick extraction by an alkaline silicate magma, which underwent exsolution of carbonaceous fluid leaving the olivine nephelinite magma. The lherzolite xenolith was first entrapped by the carbonaceous fluid for short period of time and then entrapped and transported by the olivine nephelinite magma to the surface at ~1.4 Ma.

Abbreviations

FMA	Fine-grained mineral aggregate
HREE	Heavy rare-earth element
HSE	Highly siderophile element
LLSVP	Large low shear velocity province
LREE	Light rare-earth element
MREE	Middle rare-earth element
P–T	Pressure–temperature
PUM	Primitive upper mantle
REE	Rare-earth element
SSC	Small-scale sublithospheric convection
TAS	Total alkali versus silica

Supplementary Information

The online version contains supplementary material available at <https://doi.org/10.1186/s40645-024-00643-w>.

Additional file 1.

Additional file 2.

Acknowledgements

We are grateful to N Ogawa, T Kawakami, and Y Sato for helpful assistance for EPMA; to H Yoshida for helpful assistance during FE-SEM-EDS analyses. We appreciate helpful assistance and instruction by S Okazaki, G McCormack, and J Webb during our stay in Cook Islands. We thank N Puna, V Tangatataia, B Bishop, T Arere, V Puapui, B Maxwell, A Simona, M Herman, M Rima, and the other staffs in The National Environment Service Cook Islands for assistance of our field work in Cook islands; and Government of the Cook Islands, Office of the Prime Minister, Research Permitting Authority, T&M Heather, Charlie Strickland, and Te Mato Vai for allowing us to collect rock samples. We acknowledge discussions with T Ishii, H Sumino, M Hamada, and I McIntosh. This manuscript was improved by comments from J Yamamoto and an anonymous reviewer.

Author contributions

NA, TKo, and AI designed the study. NA, AI, CO, and RF had field expeditions at Aitutaki Island. NA, CO, and AY conducted mineral major-element analyses. NA and KO did diffusion modeling and numerical simulations using the results of mineral major-element analyses, and conducted qualitative element analyses

for FMA, NA, TKo, and AY created elemental-distribution maps using either EPMA or X-ray analytical microscope. NA, AI, CO, and RF measured whole-rock compositions. AM and YI investigated FMA using FE-TEM-EDS. SW and TN carried out EBSD analyses to determine the crystallographic orientation of the chromian spinel grains. Raman spectroscopy was conducted by TKa. Mineral trace-element compositions were analyzed by AT, TM, and SA. NA, KO, TKo, and AI wrote basic framework of the manuscript and all authors contributed to improve the manuscript. All authors read and approved the final manuscript.

Funding

This work was supported by MEXT/JSPS KAKENHI (Japan) Grant Numbers 24K00733, 24K07189, 23H01267, 23K03544, 23H01269, 20KK0079, and JP15H05831.

Availability of data and materials

The datasets supporting the conclusions of this article are all included within the article and supplementary files.

Declarations

Competing interests

The authors declare that they have no competing interests.

Author details

¹Atmosphere and Ocean Research Institute, University of Tokyo, 5-1-5 Kashiwanoha, Kashiwa, Chiba 277-8564, Japan. ²Department of Environmental Science, Tokyo Gakugei University, 4-1-1 Nukuikita, Koganei, Tokyo 184-8501, Japan. ³Graduate School of Human and Environmental Studies, Kyoto University, Yoshida-Nihonmatsu, Sakyo, Kyoto 606-8501, Japan. ⁴Department of Earth and Planetary Sciences, Tokyo Institute of Technology, 2-12-1 Ookayama, Meguro, Tokyo 152-8551, Japan. ⁵Division of Earth and Planetary Sciences, Kyoto University, Kitashirakawa-Oiwake, Sakyo, Kyoto 606-8502, Japan. ⁶Department of Earth and Planetary Science, University of Tokyo, Tokyo 113-0013, Japan. ⁷Department of Geosciences, Faculty of Science, Shizuoka University, 836 Ohya, Suruga, Shizuoka 422-8529, Japan. ⁸Faculty of Geosciences and Civil Engineering, Kanazawa University, Kakuma, Kanazawa, Ishikawa 920-1192, Japan.

Received: 13 February 2024 Accepted: 11 June 2024

Published online: 05 July 2024

References

- Adam C, Bonneville A (2005) Extent of the South Pacific Superswell. *J Geophys Res* 110:B09408. <https://doi.org/10.1029/2004JB00346>
- Agrusta R, Arcay D, Tommasi A, Davaille A, Ribe N, Gerya T (2013) Small-scale convection in a plume-fed low-viscosity layer beneath a moving plate. *Geophys J Int* 194:591–610. <https://doi.org/10.1093/gji/ggt128>
- Aoki T, Ozawa K, Bodinier JL, Boudier F, Sato Y (2020) Thermal and decompression history of the Lanzo Massif, northern Italy: Implications for the thermal structure near the lithosphere–asthenosphere boundary. *Lithos* 372–373:105661. <https://doi.org/10.1016/j.lithos.2020.105661>
- Arai S (1987) An estimation of the least depleted spinel peridotite on the basis of olivine–spinel mantle array, Neues Jahrb. Min Monatsh 1987:347–354
- Ballmer MD, van Hunen J, Ito G, Tackley PJ, Bianco TA (2007) Non-hotspot volcano chains originating from small-scale sublithospheric convection. *Geophys Res Lett* 34:L23310. <https://doi.org/10.1029/2007GL031636>
- Becker H, Horan MF, Walker RJ, Gao S, Lorand JP, Rudnick RL (2006) Highly siderophile element composition of the Earth's primitive upper mantle: constraints from new data on peridotite massifs and xenoliths. *Geochim Cosmochim Acta* 70:4528–4550. <https://doi.org/10.1016/j.gca.2006.06.004>
- Bonechi B, Stagno V, Kono Y, Hrubak R, Ziberna L, Andreozzi GB, Perinelli C, Gaeta M (2022) Experimental measurements of the viscosity and melt structure of alkali basalts at high pressure and temperature. *Sci Rep* 12:2599. <https://doi.org/10.1038/s41598-022-06551-7>
- Bonneville A, Le Suavé R, Audin L, Clouard V, Dosso L, Gillot PY, Janney P, Jordahl K, Maamaatuaiahutapu K (2002) Arago Seamount: the missing hotspot found in the Austral Islands. *Geology* 30:1023–1026. [https://doi.org/10.1130/0091-7613\(2002\)030%3c1023:ASTMHF%3e2.0.CO;2](https://doi.org/10.1130/0091-7613(2002)030%3c1023:ASTMHF%3e2.0.CO;2)
- Bonneville A, Dosso L, Hildenbrand A (2006) Temporal evolution and geochemical variability of the South Pacific superplume activity. *Earth Planet Sci Lett* 244:251–269. <https://doi.org/10.1016/j.epsl.2005.12.037>
- Boyd FR, Nixon PH (1978) Ultramafic nodules from the Kimberley pipes, South Africa. *Geochim Cosmochim Acta* 42:1367–1382. [https://doi.org/10.1016/0016-7037\(78\)90042-X](https://doi.org/10.1016/0016-7037(78)90042-X)
- Brey GP, Köhler T (1990) Geothermobarometry in four-phase lherzolites II. New thermobarometers, and practical assessment of existing thermobarometers. *J Petrol* 31:1378–1378. <https://doi.org/10.1093/ptrology/31.6.1353>
- Brooker RA, Kjarsgaard BA (2011) Silicate-carbonate liquid immiscibility and phase relations in the system SiO₂–Na₂O–Al₂O₃–CaO–CO₂ at 0–1–2.5 GPa with applications to carbonate genesis. *J Petrol* 52:1281–1305. <https://doi.org/10.1093/ptrology/egq081>
- Bultitude RJ, Green DH (1971) Experimental study of crystal-liquid relationships at high pressures in olivine nephelinite and basanite compositions. *J Petrol* 12:121–147. <https://doi.org/10.1093/ptrology/12.1.121>
- Campbell IH, Griffiths RW (1990) Implications of mantle plume structure for the evolution of flood basalts. *Earth Planet Sci Lett* 99:79–93. [https://doi.org/10.1016/0012-821X\(90\)90072-6](https://doi.org/10.1016/0012-821X(90)90072-6)
- Campbell IH, Griffiths RW, Hill RI (1989) Melting in an Archaean mantle plume: heads it's basalts, tails it's komatiites. *Nature* 339:697–699. <https://doi.org/10.1038/339697a0>
- Carswell DA, Dawson JB (1970) Garnet peridotite xenoliths in south African kimberlite pipes and their petrogenesis. *Contrib Miner Petrol* 25:163–184. <https://doi.org/10.1007/BF00371129>
- Cherniak DJ, Dimanov A (2010) Diffusion in pyroxene, mica and amphibole. *Rev Miner Geochem* 72:641–690. <https://doi.org/10.2138/rmg.2010.72.14>
- Cherniak DJ, Liang Y (2022) Calcium diffusion in enstatite, with application to closure temperature of the Ca-in-opx thermometer. *Geochim Cosmochim Acta* 332:124–137. <https://doi.org/10.1016/j.gca.2022.06.018>
- Dasgupta R, Hirschmann M (2006) Melting in the Earth's deep upper mantle caused by carbon dioxide. *Nature* 440:659–662. <https://doi.org/10.1038/nature04612>
- Day JMD, Walker RJ, Warren JM (2017) ¹⁸⁶Os–¹⁸⁷Os and highly siderophile element abundance systematics of the mantle revealed by abyssal peridotites and Os-rich alloys. *Geochim Cosmochim Acta* 200:232–254. <https://doi.org/10.1016/j.gca.2016.12.013>
- Demouchy S, Ishikawa A, Tommasi A, Alard O, Keshav S (2015) Characterization of hydration in the mantle lithosphere: Peridotite xenoliths from the Ontong Java Plateau as an example. *Lithos* 212–215:189–201. <https://doi.org/10.1016/j.lithos.2014.11.005>
- Duncan RA, McDougall I (1976) Linear volcanism in French Polynesia. *J Volcanol Geotherm Res* 1:197–227. [https://doi.org/10.1016/0377-0273\(76\)90008-1](https://doi.org/10.1016/0377-0273(76)90008-1)
- Eguchi J, Dasgupta R (2018) Redox state of the convective mantle from CO₂-trace element systematics of oceanic basalts. *Geochem Perspect Lett* 8:17–21. <https://doi.org/10.7185/geochemlet.1823>
- Ezad IS, Dobson DP, Thomson AR, Jennings ES, Hunt SA, Brodholt JP (2022) Kelyphite textures experimentally reproduced through garnet breakdown in the presence of a melt phase. *J Petrol* 63:egac110. <https://doi.org/10.1093/ptrology/egac110>
- Falloon TJ, Green DH (1989) The solidus of carbonated, fertile peridotite. *Earth Planet Sci Lett* 94:364–370. [https://doi.org/10.1016/0012-821X\(89\)90153-2](https://doi.org/10.1016/0012-821X(89)90153-2)
- Fischer KM, Ford HA, Abt DL, Rychert CA (2010) The lithosphere–asthenosphere boundary. *Annu Rev Earth Planet Sci* 38:551–575. <https://doi.org/10.1146/annurev-earth-040809-152438>
- Fodor RV, Bauer GR, Keil K (1982) Ultramafic inclusions and megacrysts in olivine nephelinite, Aitutaki Island, Cook Islands. *NZ J Geol Geophys* 25:67–76. <https://doi.org/10.1080/00288306.1982.10422505>
- Gasparik T (1987) Orthopyroxene thermobarometry in simple and complex systems. *Contr Miner Petrol* 96:357–370. <https://doi.org/10.1007/BF00371254>
- Gasparik T (2000) An internally consistent thermodynamic model for the system CaO–MgO–Al₂O₃–SiO₂ derived primarily from phase equilibrium data. *J Geol* 108:103–119. <https://doi.org/10.1086/314389>
- Gasparik T (2003) Phase diagrams for geoscientists. Springer, Berlin

- Goto A, Yokoyama K (1988) Lherzolite inclusions in olivine nephelinite tuff from Salt Lake Crater. *Hawaii Lithos* 21:67–80. [https://doi.org/10.1016/0024-4937\(88\)90006-0](https://doi.org/10.1016/0024-4937(88)90006-0)
- Griffin WL, O'Reilly SY, Ryan CG (1999a) The composition and origin of sub-continental lithospheric mantle. In: Fei Y, Bertka CM, Mysen BO (eds) *Mantle petrology: field observations and high pressure experimentation. A tribute to Francis R. Geochemical Society, Houston*, pp 13–45
- Griffin WL, Fisher NI, Friedman J, Ryan GG, O'Reilly SY (1999b) Cr-pyroxene garnets in the lithospheric mantle 1. Compositional systematics and relations to tectonic setting. *J Petrol* 40:679–704. <https://doi.org/10.1093/ptro/40.5.679>
- Hanyu T, Dosso L, Ishizuka O, Tani K, Hanan BB, Adam C, Nakai S, Senda R, Chang Q, Tatsumi Y (2013) Geochemical diversity in submarine HIMU basalts from Austral Islands, French Polynesia. *Contrib Miner Petrol* 166:1285–1304. <https://doi.org/10.1007/s00410-013-0926-x>
- Harigane Y, Mizukami T, Morishita T, Michibayashi K, Abe N, Hirano N (2011) Direct evidence for upper mantle structure in the NW Pacific Plate: microstructural analysis of a petit-spot peridotite xenolith. *Earth Planet Sci Lett* 302:194–202. <https://doi.org/10.1016/j.epsl.2010.12.011>
- Herath P, Stern TA, Savage MK, Bassett D, Henrys S (2022) Wide-angle seismic reflections reveal a lithosphere-asthenosphere boundary zone in the subducting Pacific Plate, New Zealand. *Sci Adv* 8:eabn5697. <https://doi.org/10.1126/sciadv.abn5697>
- Herzberg C, Asimow PD (2015) PRIMELT3 MEGA.XLSM software for primary magma calculation: Peridotite primary magma MgO contents from the liquidus to the solidus. *Geochem Geophys Geosyst* 16:563–578. <https://doi.org/10.1002/2014GC005631>
- Hirschmann MM (2000) Mantle solidus: experimental constraints and the effect of peridotite composition. *Geochem Geophys Geosyst* 1:2000GC000070. <https://doi.org/10.1029/2000GC000070>
- Ibarguchi JIG, Ábalos B, Azcaraga J, Puelles P (1999) Deformation, high-pressure metamorphism and exhumation of ultramafic rocks in a deep subduction/collision setting (Cabo Ortegal, NW Spain). *J Metamorph Geol* 17:747–764. <https://doi.org/10.1046/j.1525-1314.1999.00227.x>
- Ishikawa A, Maruyama S, Komiya T (2004) Layered lithospheric mantle beneath the Ontong Java Plateau: implications from xenoliths in alnöite, Malaita, Solomon Islands. *J Petrol* 45:2011–2044. <https://doi.org/10.1093/ptro/egh046>
- Ishikawa A, Pearson DG, Dale CW (2011) Ancient Os isotope signatures from the Ontong Java Plateau lithosphere: tracing lithospheric accretion history. *Earth Planet Sci Lett* 301:159–170. <https://doi.org/10.1016/j.epsl.2010.10.034>
- Jackson MG, Halldórsson SA, Price A, Kurz MD, Konter JG, Koppers AAP, Day JMD (2020) Contrasting old and young volcanism from Aitutaki, Cook Islands: implications for the origins of the Cook-Austral volcanic chain. *J Petrol* 61:egaa037. <https://doi.org/10.1093/ptrology/egaa037>
- Jacob DE, Kronz A, Viljoen KS (2004) Cohenite, native iron and troilite inclusions in garnets from polycrystalline diamond aggregates. *Contrib Miner Petrol* 146:566–576. <https://doi.org/10.1007/s00410-003-0518-2>
- Kawakatsu H, Kumar P, Takei Y, Shinohara M, Kanazawa T, Araki E, Suyehiro K (2009) Seismic evidence for sharp lithosphere-asthenosphere boundaries of oceanic plates. *Science* 324:499–502. <https://doi.org/10.1126/science.1169499>
- Kawakatsu H, Utada H (2017) Seismic and electrical signatures of the lithosphere-asthenosphere system of the normal oceanic mantle. *Annu Rev Earth Planet Sci* 45:139–167. <https://doi.org/10.1146/annurev-earth-063016-020319>
- Klemme S, O'Neill HS (2000) The near-solidus transition from garnet lherzolite to spinel lherzolite. *Contrib Miner Petrol* 138:237–248. <https://doi.org/10.1007/s004100050560>
- Kono Y, Kenney-Benson C, Hummer D, Ohfuji H, Park C, Shen G, Wang Y, Kavner A, Manning CE (2014) Ultralow viscosity of carbonate melts at high pressures. *Nat Commun* 5:5091. <https://doi.org/10.1038/ncomms6091>
- Kushiro I, Yoder HS (1966) Anorthite-forsterite and anorthite—enstatite reactions and their bearing on the basalt—eclogite transformation. *J Petrol* 7:337–362. <https://doi.org/10.1093/ptrology/7.3.337>
- Le Bas MJ (1987) Nephelinites and carbonatites. In: Fitton JG, Upton BGJ (eds) *Alkaline igneous rocks*, vol 30. The Geological Society of London, Piccadilly, pp 13–45. <https://doi.org/10.1144/GSL.SP.1987.030.01.0>
- Le Bas MJ, Le Maitre RW, Streckeisen A, Zanettin B (1986) A chemical classification of volcanic rocks based on the total alkali–silica diagram. *J Petrol* 27:745–750. <https://doi.org/10.1093/ptrology/27.3.745>
- Le Maitre RW, Streckeisen A, Zanettin B, Le Bas MJ, Bonin B, Bateman P (2002) *Igneous rocks: a classification and glossary of terms: recommendations of the international union of geological sciences subcommission on the systematics of igneous rocks*, 2nd edn. Cambridge University Press, New York
- Lee W, Wyllie PJ (1997) Liquid immiscibility between nephelinite and carbonatite from 1.0 to 2.5 GPa compared with mantle melt compositions. *Contrib Miner Petrol* 127:1–16. <https://doi.org/10.1007/s004100050261>
- Litasov K, Taniguchi H (2002) *Mantle evolution beneath the Baikal Rift*. CNEAS monograph series, vol 5. Center for Northeast Asian Studies, Tohoku University
- McDonough WF, Sun SS (1995) The composition of the earth. *Chem Geol* 120:223–253. [https://doi.org/10.1016/0009-2541\(94\)00140-4](https://doi.org/10.1016/0009-2541(94)00140-4)
- McNutt MK, Judge AV (1990) The superswell and mantle dynamics beneath the South Pacific. *Science* 248:969–975. <https://doi.org/10.1126/science.248.4958.969>
- Moukadir A, Kornprobst J (1984) Garnet and/or spinel bearing pyroxenites in alkali basalts near Azrou (Middle Atlas, Morocco): mantle derived alumina-rich xenoliths related to the "ariegite-grospydyite" trend. *Devel Petrol* 11:179–189. <https://doi.org/10.1016/B978-0-444-42274-3.50021-4>
- Müller RD, Zahirovic S, Williams SE, Cannon J, Seton M, Bower DJ, Tetley MG, Heine C, Breton EL, Liu S, Russell SHJ, Yang T, Leonard J, Gurnis M (2019) A global plate model including lithospheric deformation along major rifts and orogens since the Triassic. *Tectonics* 38:1884–1907. <https://doi.org/10.1029/2018TC005462>
- Neal CR, Nixon PH (1985) Spinel-garnet relationships in mantle xenoliths from the Malaita Alnöites, Solomon Islands, South-Western Pacific. *Trans Geol Soc S Afr* 88:347–354
- Nickel KG (1986) Phase equilibria in the system SiO₂–MgO–Al₂O₃–CaO–Cr₂O₃ (SMACCR) and their bearing on spinel/garnet lherzolite relationships. *Neues Jahrbuch Miner Abh* 155:259–287
- Nickel KG, Green DH (1985) Empirical geothermobarometry for garnet peridotites and implications for the nature of the lithosphere, kimberlites and diamonds. *Earth Planet Sci Lett* 73:158–170. [https://doi.org/10.1016/0012-821X\(85\)90043-3](https://doi.org/10.1016/0012-821X(85)90043-3)
- Nicolas A, Poirier JP (1976) *Crystalline plasticity and solid state flow in metamorphic rocks*. Wiley, New York
- Niu Y (2004) Bulk-rock major and trace element compositions of abyssal peridotites: implications for mantle melting, melt extraction and post-melting processes beneath mid-ocean ridges. *J Petrol* 45:2423–2458. <https://doi.org/10.1093/ptrology/egh068>
- Niu Y, Hékinian R (1997) Basaltic liquids and harzburgitic residues in the Garrett Transform: a case study at fast-spreading ridges. *Earth Planet Sci Lett* 146:43–258. [https://doi.org/10.1016/S0012-821X\(96\)00218-X](https://doi.org/10.1016/S0012-821X(96)00218-X)
- Obata M, Ozawa K, Naemura K, Miyake A (2013) Isochemical breakdown of garnet in orogenic garnet peridotite and its implication to reaction kinetics. *Miner Petrol* 107:881–895. <https://doi.org/10.1007/s00710-012-0260-4>
- Obata M, Ohi S, Miyake A (2014) Experimental synthesis of isochemical kelyphite—a preliminary report. *J Miner Petrol Sci* 109:91–96. <https://doi.org/10.2465/jmps.131022a>
- O'Hara MJ, Richardson SW, Wilson G (1971) Garnet-peridotite stability and occurrence in crust and mantle. *Contrib Miner Petrol* 32:48–68. <https://doi.org/10.1007/BF00372233>
- Ozawa K (1997) P-T history of an ascending in orthopyroxene: a case Hokkaido, northern Japan. *Mem Geol Soc Jpn* 47:107–122
- Ozawa K (2004) Thermal history of the Horoman peridotite complex: a record of thermal perturbation in the lithospheric mantle. *J Petrol* 45:253–273. <https://doi.org/10.1093/ptrology/egg110>
- Paquet M, Day JMD, Brown DB, Walter CL (2022) Effective global mixing of the highly siderophile elements into Earth's mantle inferred from oceanic abyssal peridotites. *Geochim Cosmochim Acta* 316:347–362. <https://doi.org/10.1016/j.gca.2021.09.033>
- Regelous M, Weinzierl CG, Haase CM (2015) Controls on melting at spreading ridges from correlated abyssal peridotite—mid-ocean ridge basalt compositions. *Earth Planet Sci Lett* 449:1–11. <https://doi.org/10.1016/j.epsl.2016.05.017>

- Richardson SH, Erlank AJ, Hart SR (1985) Kimberlite-borne garnet peridotite xenoliths from old enriched subcontinental lithosphere. *Earth Planet Sci Lett* 75:116–128. [https://doi.org/10.1016/0012-821X\(85\)90094-9](https://doi.org/10.1016/0012-821X(85)90094-9)
- Richter FM, Parsons B (1975) On the interaction of two scales of convection in the mantle. *J Geophys Res* 80:2529–2541. <https://doi.org/10.1029/JB080i017p02529>
- Robie RA (1966) Thermodynamic properties of minerals. In: Sydney P, Clark P (eds) Handbook of physical constants, GSA memoir, vol 97. Geological Society of America, New York
- Rohrbach A, Ballhaus C, Golla-Schindler U, Ulmer P, Kamenetsky VS, Kuzmin DV (2007) Metal saturation in the upper mantle. *Nature* 449:456–458. <https://doi.org/10.1038/nature06183>
- Rohrbach A, Ballhaus C, Ulmer P, Golla-Schindler U, Schönbohm D (2011) Experimental evidence for a reduced metal-saturated upper mantle. *J Petrol* 52:717–731. <https://doi.org/10.1093/petrology/egq101>
- Rose J, Koppers AAP (2019) Simplifying age progressions within the Cook-Austral Islands using ARGUS-VI high-resolution $^{40}\text{Ar}/^{39}\text{Ar}$ incremental heating ages. *Geochem Geophys Geosyst* 20:4756–4778. <https://doi.org/10.1029/2019GC008302>
- Russell JK, Jones TJ (2023) Transport and eruption of mantle xenoliths creates a lagging problem. *Commun Earth Environ* 4:177. <https://doi.org/10.1038/s43247-023-00843-0>
- Ryan WBF, Carbotte SM, Coplan JO, O'Hara S, Melkonian A, Arko R, Weissel RA, Ferrini V, Goodwillie A, Nitsche F, Bonczkowski J, Zernsky R (2009) Global multi-resolution topography synthesis. *Geochem Geophys Geosyst* 10:Q03014. <https://doi.org/10.1029/2008GC002332>
- Rychert CA, Harmon N, Constable S, Wang S (2020) The nature of the lithosphere-asthenosphere boundary. *J Geophys Res: Solid Earth* 125:e2018JB016463. <https://doi.org/10.1029/2018JB016463>
- Schmidt MW, Weidendorfer D (2018) Carbonatites in oceanic hotspots. *Geology* 46:435–438. <https://doi.org/10.1130/G39621.1>
- Sen G, Keshav S, Bizimis M (2005) Hawaiian mantle xenoliths and magmas: composition and thermal character of the lithosphere. *Am Min* 90:871–887. <https://doi.org/10.2138/am.2005.1731>
- Smith D, Barron BR (1991) Pyroxene-garnet equilibration during cooling in the mantle. *Am Miner* 76:1950–1963
- Snortum E, Day JMD, Jackson MG (2019) Pacific lithosphere evolution inferred from Aitutaki mantle xenoliths. *J Petrol* 60:1753–1772. <https://doi.org/10.1093/petrology/egz047>
- Spera FJ (1984) Carbon dioxide in petrogenesis III: role of volatiles in the ascent of alkaline magma with special reference to xenolith-bearing mafic lavas. *Contr Miner Petrol* 88:217–232. <https://doi.org/10.1007/BF00380167>
- Stein CA, Stein S (1992) A model for the global variation in oceanic depth and heat flow with lithospheric age. *Nature* 359:123–129. <https://doi.org/10.1038/359123a0>
- Tommashi A, Ishikawa A (2014) Microstructures, composition, and seismic properties of the Ontong Java Plateau mantle root. *Geochem Geophys Geosyst* 15:e2014GC005452. <https://doi.org/10.1002/2014GC005452>
- Torsvik TH, Smethurst MA, Burke K, Steinberger B (2006) Large igneous provinces generated from the margins of the large low-velocity provinces in the deep mantle. *Geophys J Int* 167:1447–1460. <https://doi.org/10.1111/j.1365-246X.2006.03158.x>
- Tsuchiyama A (1986) Melting and dissolution kinetics: application to partial melting and dissolution of xenoliths. *J Geophys Res* 91:9395–9406. <https://doi.org/10.1029/JB091iB09p09395>
- Turner DL, Jarrard RD (1982) K-Ar dating of the Cook-Austral island chain: a test of the hot-spot hypothesis. *J Volcanol Geotherm Res* 12:187–220. [https://doi.org/10.1016/0377-0273\(82\)90027-0](https://doi.org/10.1016/0377-0273(82)90027-0)
- Yasumoto A, Yoshida K, Kuwatani T, Nakamura D, Svojtka M, Hirajima T (2018) A rapid and precise quantitative electron probe chemical mapping technique and its application to an ultrahigh-pressure eclogite from the Moldanubian Zone of the Bohemian Massif (Nové Dvory, Czech Republic). *Am Min* 103:1690–1698. <https://doi.org/10.2138/am-2018-6323CCBY>
- Yokoyama K (1980) Nikubuchi peridotite body in the sanbagawa metamorphic belt; thermal history of the 'Al-pyroxene-rich suite' peridotite body in high pressure metamorphic terrain. *Contr Miner Petrol* 73:1–13. <https://doi.org/10.1007/BF00376256>
- White WM (2010) Oceanic island basalts and mantle plumes: the geochemical perspective. *Annu Rev Earth Planet Sci* 38:133–160. <https://doi.org/10.1146/annurev-earth-040809-152450>
- Wood CP (1978) Petrology of Aitutaki, Cook Islands (Note). *N Z J Geol Geophys* 21:761–765. <https://doi.org/10.1080/00288306.1978.10425205>
- Zahirovic S, Müller RD, Seton M, Flament N (2015) Tectonic speed limits from plate kinematic reconstructions. *Earth Planet Sci Lett* 418:40–52. <https://doi.org/10.1016/j.epsl.2015.02.037>
- Ziberna L, Klemme S, Nimis P (2013) Garnet and spinel in fertile and depleted mantle: insights from thermodynamic modelling. *Contrib Miner Petrol* 166:411–421. <https://doi.org/10.1007/s00410-013-0882-5>

Publisher's Note

Springer Nature remains neutral with regard to jurisdictional claims in published maps and institutional affiliations.